INTEGRATION OF COLD
ATOM INTERFEROMETRY INS
WITH OTHER SENSORS

THESIS

Aaron Canciani, Second Lieutenant, USAF

AFIT/GE/ENG/12-07

DEPARTMENT OF THE AIR FORCE
AIR UNIVERSITY

AIR FORCE INSTITUTE OF TECHNOLOGY

Wright-Patterson Air Force Base, Ohio

AFIT/GE/ENG/12-07

INTEGRATION OF COLD
ATOM INTERFEROMETRY INS
WITH OTHER SENSORS

THESIS

Presented to the Faculty

Department of Electrical and Computer Engineering

Graduate School of Engineering and Management

Air Force Institute of Technology

Air University

Air Education and Training Command

In Partial Fulfillment of the Requirements for the

Degree of Master of Science in Electrical Engineering

Aaron Canciani, B.S.E.E.

Second Lieutenant, USAF

March 2012

AFIT/GE/ENG/12-07

INTEGRATION OF COLD
ATOM INTERFEROMETRY INS
WITH OTHER SENSORS

Aaron Canciani, B.S.E.E.

Second Lieutenant, USAF

Approved:

_____   _____

Dr. John Raquet, PhD (Chairman)   date

_____   _____

Dr Meir Pachter, PhD (Committee   date
Member)

_____   _____

Maj Kenneth Fisher, PhD (Committee   date
Member)

AFIT/GE/ENG/12-07

Abstract

Inertial navigation systems (INS) using cold-atom interferometry (CAI) are currently under development. According to Jekeli and others, these systems will have error parameters three or four orders of magnitude more accurate than current navigation grade INS. This significant increase in accuracy motivates the need to explore how these high accuracy inertial navigation systems can be integrated with other sensors. This paper focuses on methods of integrating cold atom interferometry INS with conventional navigation grade INS, as well as with GPS. The integration of CAI INS with conventional INS is done to address possible dynamic limitations of CAI INS. First, three filter frameworks for integrating cold atom INS with conventional INS are presented. These filters increase navigation accuracy by calibrating the navigation grade INS in flight. The high accuracy of the cold atom interferometry INS measurements provides observability of the navigation grade INS errors. The first filter framework makes corrections at the measurement level, and mechanizes off of the CAI INS measurements whenever they are available. The second framework makes corrections at the position level, and always mechanizes off of the navigation grade INS. The third framework makes corrections at both the position and measurement level, and always mechanizes off of the navigation grade INS.

This paper then presents the results of a six degree of freedom aircraft simulation using the proposed approaches for integrating CAI INS with conventional INS. Outages are created in the cold atom interferometry INS that coincide with high dynamic maneuvers. Simulations were conducted to determine which of the three proposed approaches to integrating CAI INS with navigation grade INS gives the most accurate solution. Correcting the INS errors at the measurement level was more accurate for short outages, and correcting errors at the position level was more accurate for long outages. Correcting at both the position and measurement level gave similar perfor-

mance to only correcting at the position level. With outage times as long as one third of the flight, the second and third frameworks were shown to increase performance by more than an order of magnitude over a navigation grade INS alone.

Next, a conventional loosely coupled INS - GPS for integrating cold atom interferometry INS with GPS is presented. The cold atom interferometry INS is used to estimate the navigation solution, with periodic GPS measurements being brought into a Kalman Filter to estimate the errors in the INS solution. The results of an aircraft simulation are then presented in order to analyze the effects of various length GPS outages. The errors using a cold atom interferometry INS are then compared to the errors of a navigation grade INS integrated in the same way. Monte Carlo analysis shows that a navigation grade INS - GPS can keep near GPS level accuracy with up to 100 second outages. The CAI INS - GPS can keep near GPS level accuracy with outages up to 1000 seconds.

Acknowledgements

I would like to thank my parents for all the support and encouragement they have given me to be an engineer. I would also like to thank my lovely fiance and soon to be wife for always being there for me.

Aaron Canciani

Table of Contents

List of Figures

List of Tables

List of Symbols

I. Introduction

1.1   Background

1.1.1   Inertial Navigation.   Navigation is the process of accurately determining position. Inertial navigation is a method of navigation that relies on the fundamental laws of motion that Newton first formulated hundreds of years ago. These laws allow position to be obtained by knowing the acceleration vector of a body at all times. Accelerometers and gyroscopes are one of the main components of a inertial navigation system. Accelerometers measure specific force. Specific force is the sum of linear acceleration and gravity. While the acceleration vector alone is enough information to determine position, instruments are not usually able to measure the acceleration vector directly. This is because the instruments do not "know" their own orientation. Instead, they simply measure accelerations along a single axis which may have any orientation in space. Gyroscopes are needed to determine this unknown orientation. Once the orientation is known, the accelerations may be correctly resolved into the desired reference frame. Gyroscopes measure angular rates of a body. A single integration of these angular rates will give the absolute angle of a body.

Inertial navigation systems consist of three accelerometers and three gyroscopes. These six instruments provide enough information to know acceleration in all three dimensions, and therefore position. Errors in an inertial navigation system will cause the system to drift over time. Current navigation grade INS systems have drifts on the order of 1 nautical mile/hour [10]. This is considered a highly accurate INS system and will cost on the order of tens of thousands of dollars.

1.1.2 Global Position System. The Global Positioning System consists of a network of satellites that orbit the Earth. These satellites each transmit a unique code, called a pseudo-range number (PRN), as well as data about the satellites orbit (ephemeris data). The PRN is a pseudo random code known by both the receiver and the satellite. By locking onto this code a receiver may determine how long it took the signal to reach the receiver. This timing information, along with the knowledge of the speed of light, as well as the satellite location, allows a receiver to calculate its distance from each of the satellites transmitting a PRN. The receiver is then able to trilaterate its location on Earth. GPS receivers are vulnerable to jamming.

1.1.3 Cold Atom Interferometry INS. A new type of inertial navigation system is currently under development which uses a technique called cold atom interferometry. It has been shown that vast improvements in accuracy over conventional INS may be achieved using CAI techniques. Performance characteristics given in [5] show that a CAI INS could theoretically be a meter per hour system. This is a significant improvement over current nautical mile per hour systems.

1.2   Cold Atom Interferometry INS Physics

The methods of using interferometry in ring laser gyroscopes has been well developed over the past several decades. These methods led to the first strapdown INS systems. Ring laser gyroscopes use counter propagating beams of light to produce interference patterns that provide rotation information [5]. A basic ring laser gyroscope is shown in Fig 1.1. The cold atom interferometer (similar conceptually to the ring laser gyroscope) utilizes counter propagating beams of atoms, as shown in Fig 1.2. The core physics principle that describes atom interferometry is de Broglie's 1924 proposition which states that at the quantum level, matter may be considered to possess wavelike properties [5]. This implies that a beam of atoms will have an associated phase. When undergoing rotation, there will be an associated phase shift. The phase shift is analogous to the Sagnac effect of the optical interferometer [5]. The
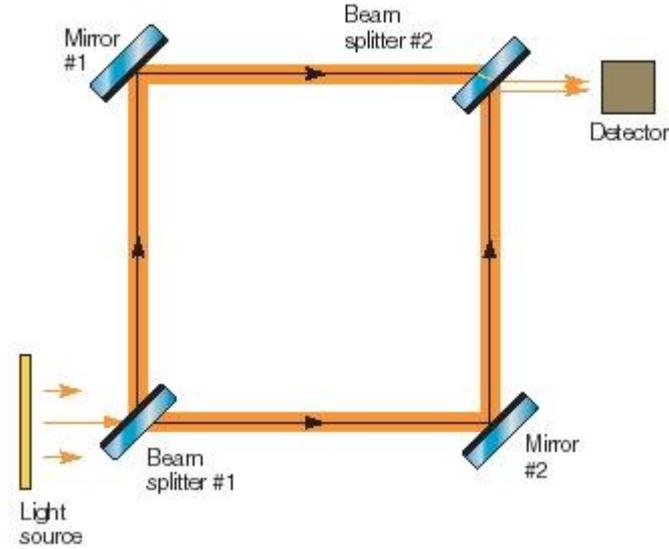
Figure 1.1:   Mach-Zehnder Interferometer

phase shift can be described as

$$\Delta\phi = \frac{4\pi\omega A}{\lambda v} \tag{1.1}$$

where the enclosed area is A, ω is rotation, λ is the wavelength of the beam, and v is the velocity. It can be seen from this equation that much greater phase shifts will be produced using atoms, because in a ring laser gyroscope the equation is divided by the speed of light, whereas in the cold atom interferometer the velocity is much lower than the speed of light. In addition, the wavelengths of the light are much higher than the wavelengths of the atom beam. These two factors show that the cold atom interferometer will be much more sensitive than a light interferometer. Calculations anticipate improvements on the order of 6×10^{10}. As in the case with a light interferometer, the phase shifts of the atomic beams will produce an interference pattern when combined. These interference patterns may be used to back out information on phase, which in turn can be used to determine angular rotation. Because of the atom's particle nature they can also be treated as inertial masses. This allows acceleration information to be obtained from the flight path of the particles.

3
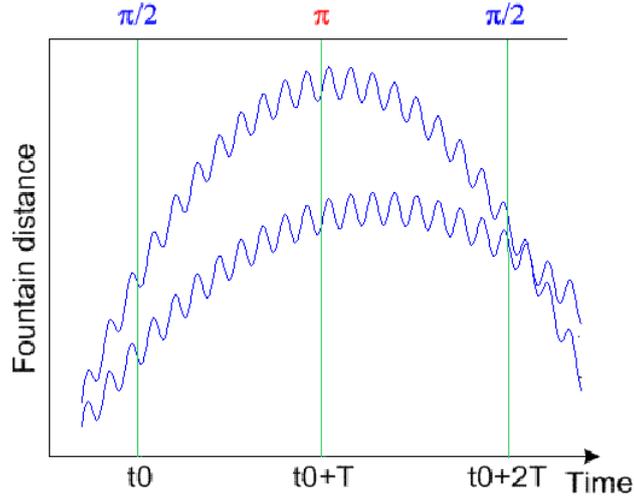
Figure 1.2:   Atoms Injected and Recombined in a Vacuum Chamber [7]

These flight paths are through a finite size vacuum chamber as shown in Fig 1.3. If the dynamics are high enough, the particle path may be outside the sensor's ability to detect when the atomic beams are recombined. This would cause the sensor to perform poorly or fail under high dynamics. This issue of dynamic performance will be addressed in the integration of a CAI INS with additional sensors.

1.3   Problem Definition

The main objective of this research is to explore the integration of a CAI INS with other sensors. Integration of conventional INS with other sensors is a well understood process. Using measurements from CAI sensors, accelerometer and gyroscope sensor models such as those given in [13] may be used to estimate and correct INS errors. The vast improvements in accuracy of a CAI INS motivates the need to re-evaluate how INS is integrated with other sensors such as GPS and multiple INS. The methods of integrating these systems as well as the performances of these systems will be significantly different in light of the highly accurate CAI INS in development.

The goal of integrating a CAI INS with an additional INS is two-fold. The first purpose is to improve navigation accuracy. This benefit would come from the high accuracy of a CAI INS. The second purpose is to improve dynamic performance.

4
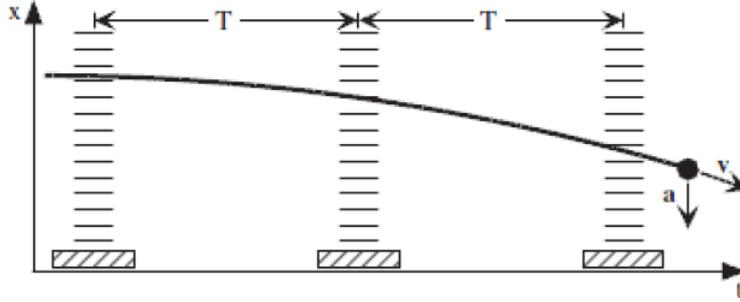
Figure 1.3:   Atoms Injected and Recombined in a Vacuum Chamber (after [3])

The need for the conventional INS arises from the concerns of CAI INS dynamic performance. A conventional INS performs well under high dynamics. In integrating these sensors together, the goal would be to create a highly accurate system that also performs well in high dynamic environments.

The goal of integrating a CAI INS with GPS is to improve system resiliency. GPS is a vulnerable system prone to interference. By integrating a GPS with a CAI INS, the risk of having a denied GPS signal would be mitigated. As with any INS-GPS system, under a GPS outage the navigation solution will begin to drift, due to the INS accumulating errors over time. The desired effect of integrating CAI INS with GPS would be to create a system whose drift is significantly slower than conventional systems during GPS outages.

1.4   Related Research

1.4.1   Integration of multiple INS.   The fusion of multiple Inertial Navigation Systems is well documented. The most common use of multiple INS is in redundancy and fault detection. Bird and McMillan describes how multiple INS can be used to enable the application of sensitive fault detection, isolation, and reconfiguration techniques [4]. Common acronyms that describe these systems are RIMU and SRIMU which stands for Redundant or Skewed Redundant Inertial Measurement Unit. These methods often involve mapping multiple IMU observations into a virtual IMU frame,

5

as described by Allerton [1]. The IMU used in these integrations are of the same performance grade. The data fusion seeks to take advantage of information obtained from IMUs in optimal configurations.

As described above, the main purpose of virtual IMU integration is not to improve accuracy but to facilitate detection of faulty observations. Bancroft [2] derives several methods to fuse multiple sensor readings into these virtual IMU frames as well as other approaches, including centralized and federated filters. Waegli discusses the possibility to reduce and to estimate the noise levels of multiple Micro-Electro-Mechanical Systems IMU systems [12]. These methods do not have any observability on sensor errors such as biases or scale factors - they can only reduce white noise. The only improvement that comes from any of the previously described methods arises from averaging white noise or detecting faults. This research differs in the purpose of improving navigation accuracy by estimating and removing INS errors.

1.4.2 Integration of CAI INS with Conventional INS. Jekeli explores the integration of a CAI INS with a conventional INS in [5]. In his paper he develops models for the acceleration and rotation measurements of a CAI INS. These measurements are shown to differ from conventional INS measurements, although he suggests that with a few reasonable assumptions they can be treated the same way. This allows him to suggest the theoretical performance of a CAI INS using common INS error parameters such as a bias and white noise. Performance parameters he presents are used in this research to create CAI INS grade measurements.

Jekeli explores the integration of a CAI INS with a low measurement duty cycle. The CAI INS considered requires a significant amount of a time to prepare the atomic cloud before it is sent through the vacuum chamber. This causes the sensor to have a sampling rate on the order of several Hertz, as opposed to the several hundred Hertz of a conventional IMU. This causes the bandwidth of the sensor to be greatly reduced. During the cooling period the sensor will not "see" the full dynamics of the platform on which it is mounted. He suggests two ways to address this issue. The first would

be to integrate the CAI INS with a conventional INS. He shows that conventional INS 50 times more accurate than current systems would be needed to give a final solution on the order of five meters per hour. The second way he suggests addressing this issue is to interleave the duty cycles of multiple CAI INS. This would increase the bandwidth of the CAI INS and allow it to capture the platform's full dynamics.

This thesis differs in the assumptions regarding the dynamic limitations of the CAI INS. While the primary limitation in dynamic performance that Jekeli considers comes from a low measurement duty cycle, this research considers absolute limits to dynamic performance. This means that when dynamics exceed a certain threshold, the sensor fails. One example of an absolute limit is a failure caused by the beam of atoms being outside the view of the sensor. Other possible failures caused by exceeding an absolute dynamic level could exist such as a 2π phase ambiguity when the atomic beams are recombined.

1.5   Potential Applications

Integration of CAI INS systems with other sensors could greatly improve navigation accuracy in a wide array of applications. Increases in accuracy of three to four orders of magnitude could completely redefine how inertial navigation systems are used. Dependence on GPS for missions less than one hour could possibly be eliminated. On longer missions, GPS outages could become much less of a concern. Because CAI INS could have limitations operating under high dynamics, the use of a CAI INS alone on these platforms may not perform well. Therefore, the fusion of CAI INS with other sensors would be especially beneficial to air vehicles operating under high dynamics. The CAI would greatly increase accuracy during low dynamics while current systems would provide the needed availability during high dynamic situations.

1.6   Methodology

The first step in the integration of cold atom interferometry INS with other sensors was to develop the integration frameworks. These frameworks described how

the measurements from each sensor would be used and combined. Next, software in MATLAB was written which implemented these frameworks. Because this system is first being tested on a theoretical level, a simulation environment was needed. The first step in the simulation environment was creating a realistic flight trajectory. INS measurements which result in this flight trajectory were then created. These perfect measurements were then corrupted according to the models of INS of various performance levels. The software in MATLAB was then given the corrupted measurements, and the results of the filter were compared to the true trajectory to determine performance.

1.7   Thesis Overview

Chapter 2 provides supporting mathematical background for the theory supporting INS mechanization, INS error modeling, and Kalman Filtering. Chapter 3 develops the frameworks for integrating CAI INS measurements with conventional INS and GPS. It then presents the Kalman Filter dynamics, measurements, and noise models. The overall software structure is given as well as the development of key performance parameters. Chapter 4 presents test results. Lastly, Chapter 5 presents conclusions and suggests future research.

II. Mathematical Background

2.1 Overview

This section presents the necessary background information required to understand the research being presented. It covers reference frames, Kalman filtering, and INS mechanization equations.

2.2 Reference Frames

Navigation information such as position and velocity are not complete without the use of a reference frame. Depending on the problem, different reference frames may be more mathematically convenient than others. All reference frames used in this research are Cartesian coordinate right handed, orthonormal, axis sets.

2.2.1 The Inertial Frame.

The inertial frame, also known as the i-frame, is a non rotating frame which can be defined by the fixed stars. Its origin is the center of the Earth and its vertical axis is aligned with the North Pole. Because the North Pole moves, an absolute location is defined by the WGS-84 system.

2.2.2 The Earth Frame.

The Earth frame, also known as the e-frame, is a rotating frame with its origin at the center of the Earth. The z axis is aligned with the North Pole as defined by the WGS-84 system. Its x-axis goes through the intersection of the Equator and the Greenwich meridian. The frame rotates at the rotation rate of the Earth, Ω

2.2.3 The Navigation Frame.

The navigation frame, also known as the n-frame, has its origin at a point in the vicinity of the surface of the Earth. The vertical axis always points in the direction of the local vertical. The x and y axes of the system point in the North and East directions on the Earth respectively. The origin of this frame always coincides with the location of the navigation system. Rotation of the Earth and movement of the navigation system will cause this frame to rotate at the rate ω_{en} (known as the transport rate).

2.2.4 The Body Frame.   The body frame is a navigation frame with origin fixed to the navigation system. The axis set is aligned with the roll, pitch, and yaw of the aircraft. The x axis is out of the noise of the aircraft, the y axis is out of the right wing, and the z axis is out of the bottom of the aircraft, perpendicular to the first two. This is the frame in which all measurements from accelerometers and gyroscopes are initially resolved. Measurements in this frame must be converted into frames useful for navigation, such as the navigation frame. The angles between the body frame and the navigation frame provide the information needed to make these conversions.

2.3 Inertial Navigation System Mechanization

This section closely follows [10]. Inertial system mechanization depends on the reference frame being utilized. The frame which will be used for this analysis will be the local level frame, also known as the navigation frame. The acceleration in the navigation frame, with respect to the earth, is

$$\dot{\mathbf{v}}_e^n = \mathbf{f}^n - (2\boldsymbol{\omega}_{ie}^n + \boldsymbol{\omega}_{en}^n) \times \mathbf{v}_e^n + \mathbf{g}_l^n \tag{2.1}$$

This equation can be thought of as the sum of three forces. The force vector $\mathbf{f}^n$ includes the forces measured by the accelerometers, expressed in the navigation frame. The second term, $(2\boldsymbol{\omega}_{ie}^n + \boldsymbol{\omega}_{en}^n) \times \mathbf{v}_e^n$, is an apparent force caused by navigating in a rotating reference frame, known as a Coriolis acceleration. It is the cross product of the object angular rate with its velocity. This angular rate is a sum of the turn rate of the Earth, $\boldsymbol{\omega}_{ie}^n$ and the turn rate of the local geographic frame, also known as the transport rate, $\boldsymbol{\omega}_{en}^n$. These two vectors are functions of the latitude and longitude on Earth, L and λ, as well as velocity, v, i.e.,

$$\boldsymbol{\omega}_{ie}^n = \begin{bmatrix} \Omega cosL & 0 & -\Omega sinL \end{bmatrix}^T \tag{2.2}$$

10

$$\boldsymbol{\omega}_{en}^n = \begin{bmatrix} \dot{\lambda}cosL & -\dot{L} & -\dot{\lambda}sinL \end{bmatrix}^T \tag{2.3}$$

Eq 2.3 can be rewritten as a function of the navigation frame velocity as

$$\omega_{en}^n = \begin{bmatrix} \frac{v_e}{R_0+h} & \frac{-v_n}{R_0+h} & \frac{-v_e tanL}{R_0+h} \end{bmatrix}^T \tag{2.4}$$

where R_0 is the radius of the Earth, v_e and v_n are the North and East velocities, h is height above the Earth, and L is latitude. The final term of Eq 2.1 is the local gravity vector, $\mathbf{g}_l^n$. This vector is the sum of the mass attraction vector $\mathbf{g}$ and the centripetal acceleration caused by the Earth's rotation, i.e.,

$$\mathbf{g}_l^n = g - \boldsymbol{\omega}_{ie} \times \begin{bmatrix} \boldsymbol{\omega}_{ie} \times R_0 \end{bmatrix} \tag{2.5}$$

which may be rewritten as

$$\mathbf{g}_l^n = g - \frac{\Omega(R_0 + h)}{2} \begin{bmatrix} sin2L \\ 0 \\ (1 + cos2L) \end{bmatrix} \tag{2.6}$$

The final navigation equations in component form are then

$$\dot{v}_N = f_N - 2\Omega v_E sinL + \frac{(v_N v_D - v_E^2 tanL)}{(R_0 + h)} + \xi g \tag{2.7}$$

$$\dot{v}_E = f_E - 2\Omega(v_N sinL + v_D cosL) + \frac{v_E}{(R_0 + h)}(v_D + v_N tanL) - \eta g \tag{2.8}$$

$$\dot{v}_D = f_D - 2\Omega v_e cosL - \frac{(v_E^2 + v_n^2)}{(R_0 + h)} + g \tag{2.9}$$

where f_N, f_E, and f_D are measured specific forces in the North, East, and down directions. ξ and η are components of gravity in the North and East directions. Latitude, longitude, and height rates are given by

$$\dot{L} = \frac{v_N}{(R_0 + h)} \tag{2.10}$$

$$\dot{\lambda} = \frac{v_E sec L}{(R_0 + h)} \tag{2.11}$$

$$\dot{h} = -v_D \tag{2.12}$$

In Eq 2.1 the forces were expressed in the navigation frame. The readings from an accelerometer, however, are not given in the navigation frame. An accelerometer outputs accelerations in a body frame. Eq 2.1 must therefore be rewritten as

$$\dot{\mathbf{v}}_e^n = \mathbf{C}_b^n \mathbf{f}^b - \left[2\boldsymbol{\omega}_{ie}^n + \boldsymbol{\omega}_{en}^n \right] \times \mathbf{v}_e^n + \mathbf{g}_l^n \tag{2.13}$$

where the direction cosine matrix (DCM), given as C_b^n, is used to resolve the measured body forces into the navigation frame. It is described by the differential equation

$$\dot{\mathbf{C}}_b^n = \mathbf{C}_b^n \boldsymbol{\Omega}_{nb}^b \tag{2.14}$$

The matrix Ω_{nb}^b is the skew symmetric form of the vector ω_{nb}^b, which is the angular rate of change of the body with respect to the navigation frame. This angular rate of change is the sum of the measured angular rates with the Earth's angular rate as well as the angular rate of the navigation frame.

$$\boldsymbol{\omega}_{nb}^b = \boldsymbol{\omega}_{ib}^b - \mathbf{C}_n^b [\boldsymbol{\omega}_{ie}^n + \boldsymbol{\omega}_{en}^n] \tag{2.15}$$

2.4   Strapdown System Error Equations

The development of error equations is necessary for the design of filters. To optimally combine data from multiple INS systems or a INS/GPS system, the filter must be told what the expected error is for all time. The error equations provide this information to the filter. They are developed here using perturbation analysis [5].

2.4.1   Attitude Errors.   The true orientation of a body in a strapdown system is represented by $\mathbf{C}_b^n$. In any real system, however, the orientation will contain errors. The computer only has access to this estimated state, denoted $\tilde{\mathbf{C}}_b^n$. The matrix $\mathbf{B}$ in

Eq 2.16 relates the true and estimated direction cosine matrices.

$$\tilde{\mathbf{C}}_b^n = \mathbf{B}\mathbf{C}_b^n \tag{2.16}$$

If the misalignment angles are small the matrix $\mathbf{B}$ may be represented as the skew symmetric matrix

$$\mathbf{B} = [\mathbf{I} - \boldsymbol{\Psi}] \tag{2.17}$$

$\mathbf{I}$ is a 3 x 3 identity matrix and $\boldsymbol{\Psi}$ is given by Eq 2.18 where γ, α, and β are the attitude errors. In a space stabilized system these errors would by the physical misalignments of the instruments with respect to their given axes.

$$\boldsymbol{\Psi} = \begin{bmatrix} 0 & -\delta\gamma & \delta\beta \\ \delta\gamma & 0 & -\delta\alpha \\ -\delta\beta & \delta\alpha & 0 \end{bmatrix} \tag{2.18}$$

Substituting Eq 2.17 into Eq 2.16 gives

$$\tilde{\mathbf{C}}_n^n = [\mathbf{I} - \boldsymbol{\Psi}]\mathbf{C}_b^n \tag{2.19}$$

Solving for Ψ and differentiating this equation gives

$$\dot{\boldsymbol{\Psi}} = -\dot{\tilde{\mathbf{C}}}_b^n \mathbf{C}_b^{nT} - \tilde{\mathbf{C}}_b^n \dot{\mathbf{C}}_b^{nT} \tag{2.20}$$

By combining Eq 2.14 and 2.15 the matrix $\mathbf{C}_b^n$ can be shown to propagate according to

$$\dot{\mathbf{C}}_b^n = \tilde{\mathbf{C}}_b^n \boldsymbol{\Omega}_{ib}^b - \boldsymbol{\Omega}_{in}^n \mathbf{C}_b^n \tag{2.21}$$

The estimated $\mathbf{C}_b^n$ matrix, $\tilde{\mathbf{C}}_b^n$ propagates the same way using the estimated absolute body rates $\tilde{\boldsymbol{\Omega}}_{ib}^b$ and the estimated navigation frame rate $\tilde{\boldsymbol{\Omega}}_{in}^n$

$$\dot{\tilde{\mathbf{C}}} = \tilde{\mathbf{C}}_b^n \tilde{\boldsymbol{\Omega}}_{ib}^b - \tilde{\boldsymbol{\Omega}}_{in}^n \tilde{\mathbf{C}}_b^n \tag{2.22}$$

Plugging Eq 2.21 and 2.22 into Eq 2.20 gives

$$\dot{\boldsymbol{\Psi}} = -\tilde{\mathbf{C}}_b^n \tilde{\boldsymbol{\Omega}}_{ib}^b \mathbf{C}_b^{nT} + \tilde{\boldsymbol{\Omega}}_{in}^n \tilde{\mathbf{C}}_b^n \mathbf{C}_b^{nT} + \tilde{\mathbf{C}}_b^n \boldsymbol{\Omega}_{ib}^b \mathbf{C}_b^{nT} - \tilde{\mathbf{C}}_b^n \mathbf{C}_b^{nT} \tilde{\boldsymbol{\Omega}}_{in}^n \qquad (2.23)$$

Simplifying yields

$$\dot{\boldsymbol{\Psi}} = -\tilde{\mathbf{C}}_b^n [\tilde{\boldsymbol{\Omega}}_{ib}^b - \boldsymbol{\Omega}_{ib}^b] \mathbf{C}_b^{nT} + \tilde{\boldsymbol{\Omega}}_{in}^n \tilde{\mathbf{C}}_b^n \mathbf{C}_b^{nT} - \tilde{\mathbf{C}}_b^n \mathbf{C}_b^{nT} \tilde{\boldsymbol{\Omega}}_{in}^n \qquad (2.24)$$

Substituting Eq 2.19 into Eq 2.24 gives

$$\dot{\boldsymbol{\Psi}} = -[\mathbf{I} - \boldsymbol{\Psi}] \mathbf{C}_b^n [\tilde{\boldsymbol{\Omega}}_{ib}^b - \boldsymbol{\Omega}_{ib}^b] \mathbf{C}_b^{nT} + \tilde{\boldsymbol{\Omega}}_{in}^n [\mathbf{I} - \boldsymbol{\Psi}] \mathbf{C}_b^n \mathbf{C}_b^{nT} - [\mathbf{I} - \boldsymbol{\Psi}] \mathbf{C}_b^n \mathbf{C}_b^{nT} \boldsymbol{\Omega}_{in}^n \qquad (2.25)$$

Expressing the differences between estimated values and true values as $\partial \boldsymbol{\Omega}_{in}$ and $\partial \boldsymbol{\Omega}_{ib}$ and ignoring error product terms gives

$$\dot{\boldsymbol{\Psi}} \approx \boldsymbol{\Psi} \boldsymbol{\Omega}_{in}^n - \boldsymbol{\Omega}_{in}^n \boldsymbol{\Psi} + \partial \boldsymbol{\Omega}_{in}^n - \mathbf{C}_b^n \partial \boldsymbol{\Omega}_{ib}^b \mathbf{C}_b^{nT} \qquad (2.26)$$

This can be expressed in vector form as

$$\dot{\psi} \approx -\boldsymbol{\omega}_{in}^n \times \psi + \partial \boldsymbol{\omega}_{in}^n - \mathbf{C}_b^n \partial \boldsymbol{\omega}_{ib}^b \qquad (2.27)$$

2.4.2 Velocity and Position Errors.   As shown previously, the acceleration, or time derivative of velocity, is given by

$$\dot{\mathbf{v}}_e^n = \mathbf{C}_b^n \mathbf{f}^b - (2\boldsymbol{\omega}_{ie}^n + \boldsymbol{\omega}_{en}^n) \times \mathbf{v}_e^n + \mathbf{g}_l^n \qquad (2.28)$$

which may be rewritten in terms of the estimated quantities, which are the quantities a computer would know. This gives

$$\dot{\tilde{\mathbf{v}}}_e^n = \tilde{\mathbf{C}}_b^n \tilde{\mathbf{f}}^b - (2\tilde{\boldsymbol{\omega}}_{ie}^n + \tilde{\boldsymbol{\omega}}_{en}^n) \times \tilde{\mathbf{v}}_e^n + \tilde{\mathbf{g}}_l^n \qquad (2.29)$$

Taking the difference of the true and estimated velocity equations yields

$$\partial \dot{\mathbf{v}} = \tilde{\mathbf{C}}_b^n \tilde{\mathbf{f}}^b - \mathbf{C}_b^n \mathbf{f}^b - (2\tilde{\boldsymbol{\omega}}_{ie}^n + \tilde{\boldsymbol{\omega}}_{en}^n) \times \tilde{\mathbf{v}} + (2\boldsymbol{\omega}_{ie}^n + \boldsymbol{\omega}_{en}^n) \times v + \tilde{\mathbf{g}}_l - \mathbf{g}_l \qquad (2.30)$$

Denoting estimated minus true values as ∂ and substituting $\tilde{\mathbf{C}}_b^n = [\mathbf{I} - \boldsymbol{\Psi}]\mathbf{C}_b^n$ as well as ignoring the products of error terms gives

$$\partial \dot{\mathbf{v}} \approx -\boldsymbol{\Psi}\mathbf{C}_b^n \mathbf{f}^b + \mathbf{C}_b^n \partial \mathbf{f}^b - (2\boldsymbol{\omega}_{ie}^n + \boldsymbol{\omega}_{en}^n) \times \partial \mathbf{v} - (2\partial \boldsymbol{\omega}_{ie}^n + \partial \boldsymbol{\omega}_{en}^n) \times \mathbf{v} - \partial \mathbf{g} \qquad (2.31)$$

Several simplifying assumptions can be made. If gravity is assumed to be known and Coriolis terms ignored this can further be reduced to

$$\partial \dot{\mathbf{v}} \approx [\mathbf{f}^n \times]\psi + \mathbf{C}_b^n \partial \mathbf{f}^b \qquad (2.32)$$

Position errors may be represented as

$$\partial \dot{\mathbf{p}} = \partial \mathbf{v} \qquad (2.33)$$

When broken into component form these 9 equations are referred to as the Pinson Error Model [10]. The matrix form of this model may be found in Chapter 3.

2.5 *Accelerometer and Gyroscope Models*

The modeling of INS accelerometers and gyroscopes is needed for the integration of two INS systems. These models are used in the Kalman filters which optimally combine information from both system dynamics and measurements. Models given below are based on [13].

2.5.1 Accelerometer Model.   The accelerometer measurement is modeled as

$$\ddot{a}_x = \ddot{a}_{x_{true}} + b_{a_x} + (1 + SF_{a_x})\ddot{a}_{x_{true}} + ASF_{a_x}|\ddot{a}_{x_{true}}| + NSF_{a_x}\ddot{a}_{x_{true}}^2 + w_{a_x} \qquad (2.34)$$

$$\ddot{a}_y = \ddot{a}_{y_{true}} + b_{a_y} + (1 + SF_{a_y})\ddot{a}_{y_{true}} + ASF_{a_y}|\ddot{a}_{y_{true}}| + NSF_{a_y}\ddot{a}_{y_{true}}^2 + w_{a_y} \quad (2.35)$$

$$\ddot{a}_z = \ddot{a}_{z_{true}} + b_{a_z} + (1 + SF_{a_z})\ddot{a}_{z_{true}} + ASF_{a_z}|\ddot{a}_{z_{true}}| + NSF_{a_z}\ddot{a}_{z_{true}}^2 + w_{a_z} \quad (2.36)$$

$\ddot{a}_x$, $\ddot{a}_y$, and $\ddot{a}_z$ are the accelerometer measured values. These measurements consist of the true values, $\ddot{a}_{x_{true}}$, $\ddot{a}_{y_{true}}$, and $\ddot{a}_{z_{true}}$, as well as several errors. These erors, described below, consist of a time correlated bias b_a, a scale factor SF_a, an asymmetric scale factor ASF_a, a non linear scale factor NSF_a, and white noise w_a.

2.5.2 Gyroscope Model. The gyroscope model is the same as the accelerometer model. The gyroscope error is modeled as

$$\dot{\theta}_x = \ddot{\theta}_{x_{true}} + b_{\theta_x} + (1 + SF_{\theta_x})\ddot{\theta}_{x_{true}} + ASF_{\theta_x}|\ddot{\theta}_{x_{true}}| + NSF_{\theta_x}\ddot{\theta}_{x_{true}}^2 + w_{\theta_x} \quad (2.37)$$

$$\dot{\theta}_y = \ddot{\theta}_{y_{true}} + b_{\theta_y} + (1 + SF_{\theta_y})\ddot{\theta}_{y_{true}} + ASF_{\theta_y}|\ddot{\theta}_{y_{true}}| + NSF_{\theta_y}\ddot{\theta}_{y_{true}}^2 + w_{\theta_y} \quad (2.38)$$

$$\dot{\theta}_z = \ddot{\theta}_{z_{true}} + b_{\theta_z} + (1 + SF_{\theta_z})\ddot{\theta}_{z_{true}} + ASF_{\theta_z}|\ddot{\theta}_{z_{true}}| + NSF_{\theta_z}\ddot{\theta}_{z_{true}}^2 + w_{\theta_z} \quad (2.39)$$

$\ddot{\theta}_x$, $\ddot{\theta}_y$, and $\ddot{\theta}_z$ are the accelerometer measured values. These measurements consist of the true values, $\ddot{\theta}_{x_{true}}$, $\ddot{\theta}_{y_{true}}$, and $\ddot{\theta}_{z_{true}}$, as well as several errors. These errors, described below, consist of a time correlated bias b_θ, a scale factor SF_θ, an asymmetric scale factor ASF_θ, a non linear scale factor NSF_θ, and white noise w_θ. The time correlated biases b_a and b_θ are modeled as first order Gauss-Markov processes defined by a time constant τ and standard deviation σ_{bias} [6]. They are both described by the statistics

$$E[b] = 0 \quad (2.40)$$

$$E[b^2] = \sigma_{bias}^2 \quad (2.41)$$

16

Table 2.1:   Conventional and CAI INS parameter values [5]

Conventional Accelerometer White Noise Variance	$(5 \times 10^{-5} m/s^2/\sqrt{Hz})^2$
Conventional Gyroscope White Noise Variance	$(6 \times 10^{-2} deg/h/\sqrt{Hz})^2$
CAI Accelerometer White Noise Variance	$(3 \times 10^{-8} m/s^2/\sqrt{Hz})^2$
CAI Gyroscope White Noise Variance	$(1.2 \times 10^{-4} deg/h/\sqrt{Hz})^2$
Conventional Accelerometer Bias Variance	$(2 \times 10^{-4} m/s^2)^2$
Conventional Gyroscope Bias Variance	$(3 \times 10^{-3} deg/h)^2$
Conventional Accelerometer Scale Factors (1 σ value)	300ppm
Conventional Gyroscope Scale Factors (1 σ value)	300ppm

The time correlated bias has a time constant τ which describes how long it takes to decorrelate with itself. The relationship between the desired bias sigma and the driving white noise strength q is

$$q = \frac{2\sigma^2}{\tau} \tag{2.42}$$

The additive white noises w_a and w_g are assumed to be normally distributed with zero mean and covariance given by

$$E[w_a^2] = \sigma_a^2 \tag{2.43}$$

$$E[w_\theta^2] = \sigma_\theta^2 \tag{2.44}$$

The linear scale factor errors, SF_a and SF_θ, are errors that grow linearly with the sensor input. The non linear scale factor, NSF_a and NSF_θ, are errors that grow with the square of the input. The asymmetric scale factor, ASF_a, and ASF_θ change the scale factor depending on whether the input is positive or negative. All scale factor errors are modeled as zero-mean Gaussian constants with variances given in Table 2.1. A depiction of these errors is given in Fig 2.1 [13].

2.6   Kalman filtering

2.6.1   Linear Kalman filtering.   Kalman filtering is used to estimate the solution to a linear stochastic differential equation. It is a recursive, optimal data processing algorithm [6]. Being recursive, it only relies only on the previous estimate

17
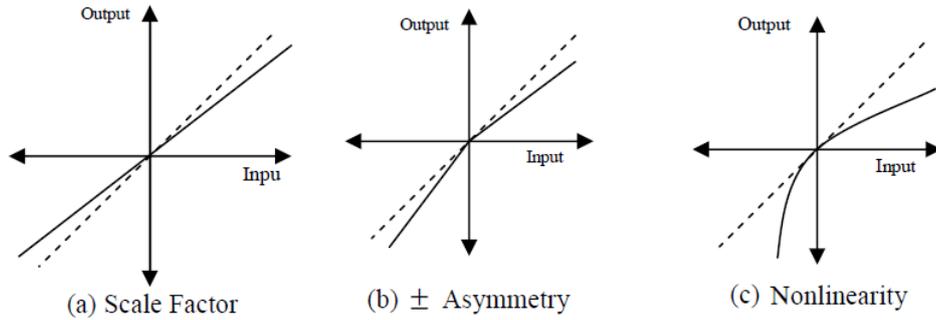
Figure 2.1:   Scale Factor Examples for INS Instrument Error Models

to create a new estimate. This makes the algorithm practical for real world use. The algorithm is also statistically optimal, meaning if all assumptions are met, the algorithm gives the best possible estimate of all states. A key assumption of Kalman filtering is that there exists an accurate and linear mathematical model of the true system. Because few things in the real world are linear, an accurate linear model is rarely possible. An additional key assumption is that that the random processes being described are Gaussian. In light of the violations of these assumptions, an optimal estimate is difficult to actually obtain. Many methods of modifying and tuning a Kalman filter exist in order to achieve the best solution.

   2.6.1.1 State Model Equations.   The description given below of the Kalman filter equations follows [8], which is based on [6, 11]. The form of the system model must satisfy the linear equation

$$\dot{\mathbf{x}}(t) = \mathbf{F}(t)\mathbf{x}(t) + \mathbf{B}(t)u(t) + \mathbf{G}(t)\mathbf{w}(t) \tag{2.45}$$

where $\mathbf{x}(t)$ is the n-dimensional system state vector, $\mathbf{F}(t)$ is the n-by-n system dynamics matrix, $\mathbf{B}(t)$ is the n-by-r control input matrix, $\mathbf{u}(t)$ is the r-dimensional control input matrix, $\mathbf{G}(t)$ is the n-by-s noise input matrix, and $\mathbf{w}(t)$ is the s-dimensional dynamics driving noise vector. The noise vector $\mathbf{w}(t)$ is a random process which is

18

white Gaussian and described by

$$E\{\mathbf{w}(t)\} = 0 \tag{2.46}$$

$$E\{\mathbf{w}(t)\mathbf{w}^T(t')\} = \mathbf{Q}(t)\delta(t - t') \tag{2.47}$$

The solution to Eq 2.45, found in [6] is given by

$$\mathbf{x}(t_{i+1}) = \mathbf{\Phi}(t_{i+1}, t_i)\mathbf{x}(t_i) + \left[\int_{t_i}^{t_{i+1}} \mathbf{\Phi}(t_{i+1}, \tau)\mathbf{G}(\tau)\delta\beta(\tau)\right] \tag{2.48}$$

The vector β is a Brownian motion process with dispersion Q and $\mathbf{\Phi}(t_{i+1}, t_i)$ is the state transition matrix from time t_i to t_{i+1}. In discrete time the $\mathbf{\Phi}$ matrix is given by

$$\mathbf{\Phi}(t_{i+1}, t_i) = \mathbf{\Phi}(\Delta t) = e^{\mathbf{F}\Delta t} \tag{2.49}$$

The discrete time form of Eq 2.45 is given by

$$\mathbf{x}(t_{i+1}) = \mathbf{\Phi}(t_{i+1}, t_i)\mathbf{x}(t_i) + \mathbf{w}_d(t_i) \tag{2.50}$$

$\mathbf{w}_d$ is a random process given by

$$\mathbf{w}_d(t_i) = \int_{t_i}^{t_{i+1}} \mathbf{\Phi}(t_{i+1}, \tau)\mathbf{G}(\tau)\delta\beta(\tau) \tag{2.51}$$

with statistics

$$E\{\mathbf{w}_d(t_i)\} = 0 \tag{2.52}$$

$$E\{\mathbf{w}_d(t_i)\mathbf{w}_d^T(t_i)\} = \mathbf{Q}_d(t_i) = \int_{t_i}^{t_{i+1}} \mathbf{\Phi}(t_{i+1}, \tau)\mathbf{G}(\tau)\mathbf{Q}(\tau)\mathbf{G}^T(\tau)\mathbf{\Phi}^T(t_{i+1}, \tau)\delta\tau \tag{2.53}$$

$$E\{\mathbf{w}_d(t_i)\mathbf{w}_d^T(t_j)\} = 0, t_i \neq t_j \tag{2.54}$$

2.6.1.2 Measurement Model Equations. Kalman filtering allows measurements with a degree of uncertainty to be incorporated into the optimal state estimate. The measurements must be expressed as a linear combination of the sys-

tem states. The measurement model is

$$\mathbf{z}(t_i) = \mathbf{H}(t_i)\mathbf{x}(t_i) + \mathbf{v}(t_i) \tag{2.55}$$

The $\mathbf{H}$ matrix describes the mapping from the system states to the measurement value. The random variable $\mathbf{v}(t_i)$ is the measurement noise, modeled as white Gaussian noise with statistics

$$E\{\mathbf{v}(t_i)\} = 0 \tag{2.56}$$

$$E\{\mathbf{v}(t_i)\mathbf{v}^T(t_j)\} = \left\{ \begin{array}{cc} \mathbf{R}(t_i) & \text{for} \quad t_i = t_j \\ 0 & \text{for} \quad t_i \neq t_j \end{array} \right\}. \tag{2.57}$$

2.6.1.3 Kalman filter Algorithm. The Kalman filter is a recursive algorithm. There are two main steps to the algorithm - propagate and update. The propagate step moves the current state estimate forward in time based off of the system model. The update step takes into account the new information made available by a measurement and creates a new optimal state estimate with this information. The system and measurement models are stochastic, and therefore all system states are random processes. Because these random processes are assumed to be Gaussian, only two moments of the random processes must be calculated, the mean and the covariance. The propagation of these two moments, found in [6], with the input term ignored, are given by

$$\hat{\mathbf{x}}(t_i^-) = \mathbf{\Phi}(t_i, t_{i-1})\hat{\mathbf{x}}(t_{i-1}^+) \tag{2.58}$$

$$\mathbf{P}(t_i^-) = \mathbf{\Phi}(t_i, t_{i-1})\mathbf{P}(t_{i-1}^+)\mathbf{\Phi}^T(t_i, t_{i-1}) + \mathbf{G}_d(t_{i-1})\mathbf{Q}_d(t_{i-1})\mathbf{G}_d^T(t_{i-1}) \tag{2.59}$$

When an update is incorporated into the system, it must be optimally mixed with the current state estimate. This is done by weighting the measurement residual with the Kalman gain, K. This gain, found in [6], is given by

$$\mathbf{K}(t_i) = \mathbf{P}(t_i^-)\mathbf{H}^T(t_i)[\mathbf{H}(t_i)\mathbf{P}(t_i^-)\mathbf{H}^T(t_i) + \mathbf{R}(t_i)]^{-1} \tag{2.60}$$

20

The measurement residual is simply the difference between the expected measurement and the actual measurement. The residual is given by [6]

$$\mathbf{r}(t_i) = \mathbf{z}_i - \mathbf{H}(t_i)\hat{\mathbf{x}}(t_i^+) \tag{2.61}$$

To complete the update process the mean of the state estimate is calculated by adding the weighted residual to the previous state. The new covariance is calculated in the same manner, with the H matrix included to take into account which states are mapped to the measurement output [6].

$$\hat{\mathbf{x}}(t_i^+) = \hat{\mathbf{x}}(t_i^-) + \mathbf{K}(t_i)\mathbf{r}(t_i) \tag{2.62}$$

$$\mathbf{P}(t_i^+) = \mathbf{P}(t_i^-) - \mathbf{K}(t_i)\mathbf{H}(t_i)\mathbf{P}(t_i^-) \tag{2.63}$$

2.6.2 Non Linear Kalman filtering.   The requirement of a linear mathematical model to achieve an optimal state estimate is a strict requirement that is often not possible in real world situations. Extended Kalman filtering is a variation of Kalman filtering that attempts to lessen the difficulty of meeting this requirement. An extended Kalman filter linearises a non-linear mathematical model at each step in time. This allows a non linear system model to be used while at the same time allowing the use of the linear Kalman filter equations. The non linear mathematical model of a system is given by

$$\hat{\mathbf{x}} = \mathbf{f}[\mathbf{x}(t), u(t), t] + \mathbf{G}\mathbf{w}(t) \tag{2.64}$$

The non-linear measurement model is given by

$$\mathbf{z}(t_i) = \mathbf{h}[\mathbf{x}(t_i), t_i] + \mathbf{v}(t_i) \tag{2.65}$$

Perturbation techniques are used to allow the Kalman filtering equations to be used with non-linear system models. The system state $\mathbf{x}(t)$ is defined as being the sum of

a nominal state $\bar{\mathbf{x}}(t)$ plus an error state $\delta\hat{\mathbf{x}}(t)$

$$\hat{\mathbf{x}} = \bar{\mathbf{x}}(t) + \delta\hat{\mathbf{x}}(t) \tag{2.66}$$

The error state is what the Kalman filter will now operate on. After linearising a non-linear model this error state may be better estimated as a Gaussian random variable and solved for using the linear Kalman filter equations. The measurement model can be expressed in a similar manner. The measurement will be the sum of an expected measurement at the nominal, $\mathbf{h}[\bar{x}(t_{i+1}^-), t_{i+1}]$ plus a small perturbation due to linearising the model, as well as noise.

$$\mathbf{z}(t_{i+1}) = \mathbf{h}[\bar{\mathbf{x}}(t_{i+1}^-), t_{i+1}] + \mathbf{H}(t_{i+1})\delta\mathbf{x}(t_{i+1}) + \mathbf{v}(t_{i+1}) \tag{2.67}$$

The matrix $\mathbf{H}$ is calculated by

$$\mathbf{H}(t) = \frac{\partial\mathbf{h}}{\partial\mathbf{x}}|_{\hat{\mathbf{x}}(t),t} = \begin{bmatrix} \frac{\partial h_1}{\partial x_1} & \cdots & \frac{\partial h_1}{\partial x_n} \\ \vdots & \ddots & \vdots \\ \frac{\partial h_n}{\partial x_1} & \cdots & \frac{\partial h_n}{\partial x_n} \end{bmatrix} \tag{2.68}$$

The previously presented Kalman filter equations are then used to propagate and update the error states. At each time step the new total state must be calculated by adding the nominal state to the error state as follows

$$\bar{\mathbf{x}}(t_{i+1}^+) = \bar{\mathbf{x}}(t_{i+1}^-) + \delta\hat{\mathbf{x}}(t_{i+1}^+) \tag{2.69}$$

Because the error state is defined as the perturbation about the nominal, when a new nominal is calculated the error covariance is reset to 0.

2.6.3 Upper Diagonal Kalman filtering. The Upper Diagonal Filter (UD) Filter, is a computationally efficient form of a square root filter [6]. These filters are used when numerical precision becomes a problem. These numerical precision prob-

lems are usually caused by very accurate measurements or large ratios between the largest and smallest eigenvalues of $\mathbf{P}$. Square root filters are algebraically equivalent forms of the Kalman filter with better numerical performance. The UD filter starts by factoring the covariance matrix $\mathbf{P}$ into upper diagonal form

$$\mathbf{P}(t_i^-) = \mathbf{U}(t_i^-)\mathbf{D}(t_i^-)\mathbf{U}^T(t_i^-) \tag{2.70}$$

where $\mathbf{U}$ is upper triangular with 1's along the diagonal and $\mathbf{D}$ is diagonal. The states are propagated in the same way as the standard Kalman filter,

$$\hat{\mathbf{x}}(t_{i+1}^-) = \mathbf{\Phi}(t_{i+1}, t_i)\hat{\mathbf{x}}(t_i^+) \tag{2.71}$$

To propagate the covariance start with

$$\mathbf{P}(t_{i+1}^-) = \mathbf{\Phi}(t_{i+1}, t_i)\mathbf{P}_i^+\mathbf{\Phi}^T(t_{i+1}, t_i) + \mathbf{G}_d\mathbf{Q}_d\mathbf{G}_d^T \tag{2.72}$$

where

$$\mathbf{P}_{i+1}^- = \mathbf{U}_{i+1}^-\mathbf{D}_{i+1}^-(\mathbf{U}_{i+1}^-)^T \tag{2.73}$$

An algorithm to solve for the P_i^+ matrix can be found in [6]. This algorithm also calculates the updated state, $\mathbf{x}(t_i^+)$

III. Integration Methods for Cold Atom Interferometry INS

3.1 Overview

This section details the design of several different integration methods for CAI INS. Three methods for integrating CAI with conventional INS are presented as well as an integration method for GPS. The creation of the simulation environment as well as the derivation of key system parameter values is also covered.

3.2 Truth Model and Generation of Measurements

A set of δV and $\delta \theta$ measurements were created from real flight path data for use in this simulation. The process of going from the real flight path to these δV and $\delta \theta$ measurements used a simple model and therefore the trajectory created by mechanizing these measurements is slightly different than the true data.

3.2.1 True δV and $\delta \theta$ measurement generation.

The method used for generating true δV and $\delta \theta$ measurements started with a set of real flight data. This data consisted of Earth centered Earth fixed position. The first step was converting the ECEF data into latitudes, longitudes, and altitudes. This data was then differentiated to obtain latitude, longitude, and altitude rates. Using the radius of the Earth, these rates were then converted into NED velocities. The equivalent Earth radii, found in [10], are given by

$$
\begin{aligned}
R_m &= \frac{a(1-e^2)}{(1-e^2 sin^2\phi)^{3/2}} \\
R_p &= \frac{a}{(1-e^2 sin^2\phi)^{1/2}}
\end{aligned}
\tag{3.1}
$$

where a is the Earth's radius, e is the Earth's eccentricity, and ϕ is latitude. The NED velocities are given by

$$
\begin{aligned}
V_E &= (R_p + h)cos\phi\dot{\lambda} \\
V_N &= (R_m + h)\dot{\phi}
\end{aligned}
\tag{3.2}
$$

24

where $\dot{\phi}$ and $\dot{\lambda}$ are the latitude and longitude rates obtained by differentiating latitude and longitude, and h is height above the Earth. Yaw and pitch were then obtained using the NED velocity vectors, under the assumption that the vehicle is aligned with the velocity vectors.

$$Yaw = tan^{-1}\left(\frac{V_N}{V_E}\right)$$
$$V_{horiz} = \sqrt{V_N^2 + V_E^2}$$
$$Pitch = -tan^{-1}\left(\frac{V_D}{V_{horiz}}\right) \tag{3.3}$$

Obtaining roll is not as straightforward. There is no lateral component of specific force in the body frame. The method used was to first find the angle between the acceleration and the velocity vectors. This angle α was obtained by

$$\alpha = tan^{-1}\frac{|a \times v|}{a \cdot v} \tag{3.4}$$

Perpendicular horizontal acceleration, defined as the acceleration perpendicular to the velocity vector in the horizontal plane, was then obtained by finding the perpendicular component of the horizontal acceleration magnitude projected onto the horizontal velocity vector.

$$a_{horiz} = \sqrt{a_N^2 + a_E^2}$$
$$a_{perp} = a_{horiz}cos\alpha \tag{3.5}$$

This projection is shown in Fig 3.1. The final step is to determine the angle between this horizontal acceleration and the gravity vector given by

$$Roll = tan^{-1}\frac{a_{perp}}{g} \tag{3.6}$$

The yaw pitch and roll are first used to create a C_b^n matrix for each point in time. The yaw, pitch, and roll were then differentiated to give yaw, pitch, and roll rates. These
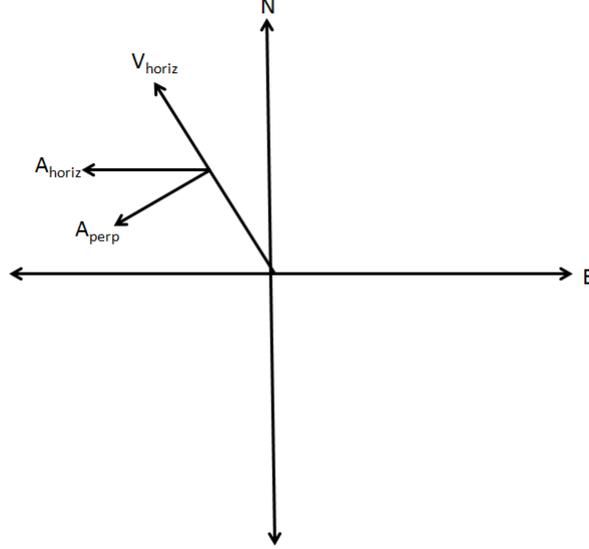
Figure 3.1:   Determining Roll Angle From Velocity and Acceleration for Creating δV and $\delta\theta$ Measurements

body rates must then be related to the gimbal rates ω_x, ω_y, and ω_z. The relation between these rates is given by

$$
\begin{pmatrix} \omega_x \\ \omega_y \\ \omega_z \end{pmatrix} = \begin{pmatrix} \dot{\phi} \\ 0 \\ 0 \end{pmatrix} + C_3 \begin{pmatrix} 0 \\ \dot{\theta} \\ 0 \end{pmatrix} + C_3 C_2 \begin{pmatrix} 0 \\ 0 \\ \dot{\Psi} \end{pmatrix} \tag{3.7}
$$

The Earth rate and transport rate were not taken into account in these conversions. This causes the trajectory generated using this method to differ from the original data. This was not an issue because the truth data used in this simulation was created by running these uncorrupted measurements through the mechanization equations. The purpose of using the original data was to get realistic measurements, not to precisely recreate the trajectory. The $\Delta\mathbf{V}$ measurements were then created by multiplying by sampling time, subtracting gravity, and converting into body frame coordinates.

$$
\Delta\mathbf{V} = \mathbf{C}_b^n \begin{pmatrix} A_N \cdot dt \\ A_E \cdot dt \\ (A_D - g) \cdot dt \end{pmatrix} \tag{3.8}
$$

26

The $\Delta\theta$ measurements were obtained by multiplying the body rates by sampling time.

$$\Delta\theta = dt \cdot \begin{pmatrix} \omega_x \\ \omega_y \\ \omega_z \end{pmatrix} \tag{3.9}$$

3.2.2   Corrupted δV and $\delta\theta$ measurement generation.   The δV and $\delta\theta$ measurements were then corrupted according to two different models. The first model was for a CAI INS. This creates a trajectory which drifts slightly from the true model. The second model was for a navigation grade INS. This trajectory drifts a great deal more than the high accuracy INS. The true, CAI INS, and navigation grade INS trajectories are shown in Fig 3.3 through Fig 3.5. Running the true ΔV and $\Delta\theta$ measurements through the mechanization equations results in the truth data shown in Fig 3.3-3.5. Note that altitude is always the same because of external barometer aiding.

3.3   Framework 1 Filter Design

The first framework the for dual INS integration will correct errors at the measurement level. Any time the CAI INS is available the mechanization will be done using these highly accurate measurements. Mechanization is the process of generating position, velocity, and attitude, from the INS ΔV and $\Delta\theta$ measurements. Simultaneously, measurements from both the CAI INS and the navigation grade INS will be brought into a Kalman Filter. This filter will estimate the errors in the navigation grade measurement. Whenever an outage occurs the mechanization must be done using the navigation grade measurements. Because the Kalman filter has estimates of the navigation grade INS errors, the measurements may be corrected before they are input into the mechanization equations. In this way, the mechanization is done using CAI INS measurements when available, and using corrected navigation grade INS measurements when CAI INS measurements are not available. Fig 3.2 shows the filter structure. The Kalman filter will estimate a solution to the equation
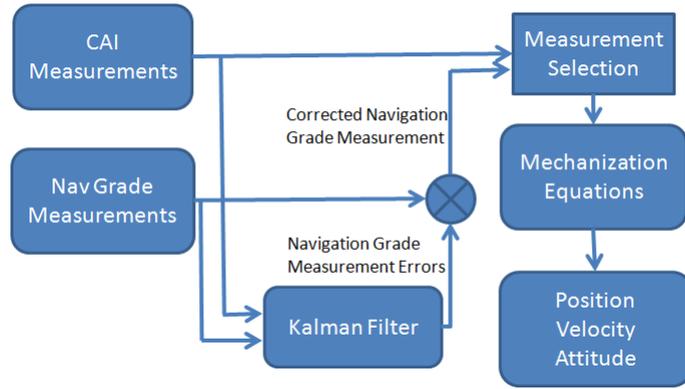
Figure 3.2:   Dual Inertial Filter Framework 1 Block Diagram

$$\dot{x} = Fx(t) + Gw(t) \tag{3.10}$$

Within the dynamics matrix, $\mathbf{F}$, the sensor errors are propagated into navigation solution errors. The matrix $\mathbf{w}$ is the noise that is entering the states of the system. The states of the implemented Kalman filter are given in Table 3.1.

Table 3.1:   Dual INS Filter States

Filter States	Description
$\mathbf{b}_a$	X,Y, and Z Accelerometer Bias
$\mathbf{b}_\theta$	X,Y, and Z Gyro Bias
$\mathbf{SF}_a$	X,Y, and Z Accelerometer Linear Scale Factor
$\mathbf{SF}_\theta$	X,Y, and Z Gyro Linear Scale Factor
$\mathbf{NSF}_a$	X,Y, and Z Accelerometer Non Linear Scale Factor
$\mathbf{NSF}_\theta$	X,Y, and Z Gyro Non Linear Scale Factor
$\mathbf{ASF}_a$	X,Y, and Z Accelerometer Asymmetric Scale Factor
$\mathbf{ASF}_\theta$	X,Y, and Z Gyro Asymmetric Scale Factor
$\mathbf{\Delta V}_{true}$	X,Y, and Z True X-Accelerometer ΔV
$\mathbf{\Delta}\theta_{true}$	X,Y, and Z True X-Gyro $\Delta\theta$

Figure 3.3:   Comparison Of True and Corrupted Flight Trajectories For A CAI Grade And Navigation Grade INS System Sample Trajectory
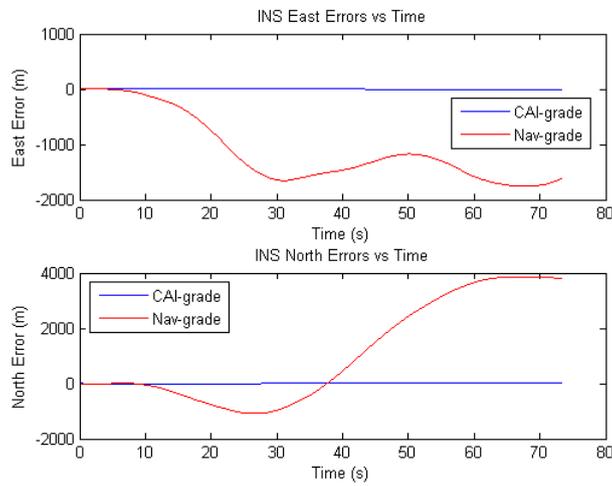
Figure 3.4:   Comparison Of True and Corrupted Altitude vs. Time For A CAI Grade And Navigation Grade INS System Sample Trajectory
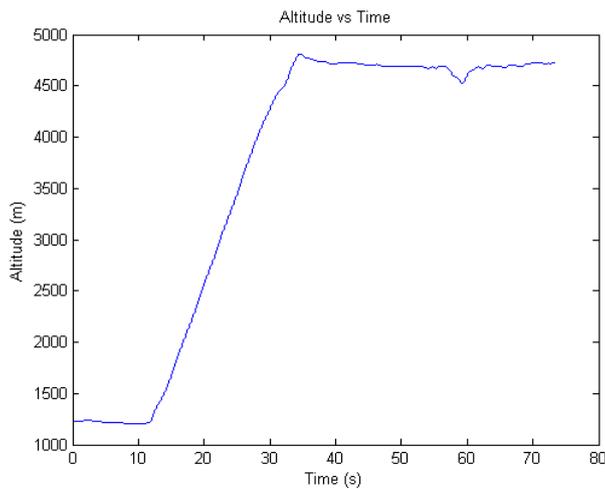
Figure 3.5:   Comparison Of CAI Grade And Navigation Grade East and North Error vs. Time For Sample Trajectory

The **F** matrix is given in Eq 3.11. The **B** matrix describes the dynamics of the time-correlated biases as first order Gauss Markov processes with time constants equal to τ.

$$\mathbf{F} = \begin{bmatrix} \mathbf{B} & 0 \\ 0 & 0 \end{bmatrix}_{30x30} \tag{3.11}$$

$$\mathbf{B} = \begin{bmatrix} -1/\tau_{ax} & 0 & 0 & \cdots \\ 0 & -1/\tau_{ay} & 0 & \cdots \\ \vdots & \vdots & \ddots & \vdots \\ 0 & \cdots & -1/\tau_{gy} & 0 \\ 0 & \cdots & 0 & -1/\tau_{gz} \end{bmatrix}_{6x6} \tag{3.12}$$

The noise vector **w** contains 12 noise sources which account for the driving noises for the accelerometer and gyroscope biases as well as the tuning noises for the ΔV_{true} and $\Delta\theta_{true}$ states. The function of these tuning noise states will be described in the measurement model section. The noise vector is given by

$$\mathbf{w} = \begin{bmatrix} \mathbf{w}_{accel}^{bias} \\ \mathbf{w}_{gyro}^{bias} \\ \mathbf{w}_{accel}^{tuning} \\ \mathbf{w}_{gyro}^{tuning} \end{bmatrix}_{12x1} \tag{3.13}$$

Where

$\mathbf{w}_{accel}^{bias}$ = x,y, and z accel time-correlated bias driving noise

$\mathbf{w}_{gyro}^{bias}$ = x,y, and z gyro time-correlated bias driving noise

$\mathbf{w}_{accel}^{tuning}$ = Accel True ΔV Tuning Noise

$\mathbf{w}_{gyro}^{tuning}$ = Gyro True $\Delta\theta$ Tuning Noise

31

The measurement model is given by the following equations, each describing three channels.

$$\Delta\mathbf{V}_{cai} = \Delta\mathbf{V}_{true} + \mathbf{w}_{a_{cai}}$$

$$\Delta\theta_{cai} = \Delta\theta_{true} + \mathbf{w}_{g_{cai}} \qquad (3.14)$$

$$\Delta\mathbf{V}_{nav} = \Delta\mathbf{V}_{true}(\mathbf{I} + \mathbf{SF} + \mathbf{NSF} + \mathbf{ASF}) + \qquad (3.15)$$

$$\mathbf{b}_{a_{nav}} + \mathbf{w}_{a_{nav}}$$

$$\Delta\theta_{nav} = \Delta\theta_{true}(\mathbf{I} + \mathbf{SF} + \mathbf{NSF} + \mathbf{ASF}) +$$

$$\mathbf{b}_{g_{nav}} + \mathbf{w}_{g_{nav}} \qquad (3.16)$$

It can be seen from the equations that the ΔV_{true} and $\Delta\theta_{true}$ states are set equal to the CAI INS measurements. The white noise of the CAI INS adds a small amount of uncertainty to these measurements. The navigation grade INS measurements are then set equal to these same ΔV_{true} and $\Delta\theta_{true}$ states with the addition of the error terms. Large tuning noises are then added to the ΔV_{true} and $\Delta\theta_{true}$ states as described previously. This makes the filter strongly trust the CAI INS measurement coming in at each time epoch. In this way the filter is able to accurately estimate the navigation grade INS errors. There are twelve measurements coming into the Kalman Filter in

all - 2 separate INS systems each with 6 channels.

$$
\mathbf{z} =
\begin{bmatrix}
\Delta V_{caix} \\
\Delta V_{caiy} \\
\Delta V_{caiz} \\
\Delta \theta_{caix} \\
\Delta \theta_{caiy} \\
\Delta \theta_{caiz} \\
\Delta V_{navx} \\
\Delta V_{navy} \\
\Delta V_{navz} \\
\Delta \theta_{navx} \\
\Delta \theta_{navy} \\
\Delta \theta_{navz}
\end{bmatrix}
\tag{3.17}
$$

The above equations lead to the following $\mathbf{H}$ matrix.

$$
\mathbf{H} =
\begin{bmatrix}
0 & 0 & 0 & 0 & \mathbf{I} \\
\mathbf{I} & \mathbf{SF} & \mathbf{NSF} & \mathbf{ASF} & \mathbf{I}
\end{bmatrix}_{12x30}
\tag{3.18}
$$

where

$$
\mathbf{SF} =
\begin{bmatrix}
\Delta V_x & 0 & 0 & 0 & 0 & 0 \\
0 & \Delta V_y & 0 & 0 & 0 & 0 \\
0 & 0 & \Delta V_z & 0 & 0 & 0 \\
0 & 0 & 0 & \Delta \theta_x & 0 & 0 \\
0 & 0 & 0 & 0 & \Delta \theta_y & 0 \\
0 & 0 & 0 & 0 & 0 & \Delta \theta_z
\end{bmatrix}
\tag{3.19}
$$

33
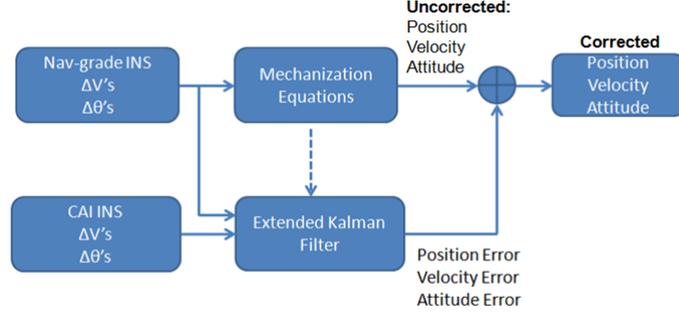
Figure 3.6: Dual Inertial Filter Framework 2 Block Diagram

$$\mathbf{NSF} = \begin{bmatrix} \Delta V_x^2 & 0 & 0 & 0 & 0 & 0 \\ 0 & \Delta V_y^2 & 0 & 0 & 0 & 0 \\ 0 & 0 & \Delta V_z^2 & 0 & 0 & 0 \\ 0 & 0 & 0 & \Delta\theta_x^2 & 0 & 0 \\ 0 & 0 & 0 & 0 & \Delta\theta_y^2 & 0 \\ 0 & 0 & 0 & 0 & 0 & \Delta\theta_z^2 \end{bmatrix} \qquad (3.20)$$

$$\mathbf{ASF} = \begin{bmatrix} |\Delta V_x| & 0 & 0 & 0 & 0 & 0 \\ 0 & |\Delta V_y| & 0 & 0 & 0 & 0 \\ 0 & 0 & |\Delta V_z| & 0 & 0 & 0 \\ 0 & 0 & 0 & |\Delta\theta_x| & 0 & 0 \\ 0 & 0 & 0 & 0 & |\Delta\theta_y| & 0 \\ 0 & 0 & 0 & 0 & 0 & |\Delta\theta_z| \end{bmatrix} \qquad (3.21)$$

Using the $\mathbf{F}$, $\mathbf{G}$, and $\mathbf{H}$ matrices, a Kalman filter can be implemented. The particular type of Kalman filter implemented is a UD filter [6]. This was needed because of the large differences in eigenvalues in the $\mathbf{w}$ matrix, which arise from large tuning noises for the true states and small driving bias noises.

3.4 Dual INS Filter Framework Two

The second proposed framework for integrating the CAI measurements is given in Fig 3.6. A Kalman filter is used to combine measurements from the CAI inertial

with the conventional inertial. This framework starts with the traditional Pinson error model and augments the filter with the states from Framework 1. The mechanization will be done using the navigation grade INS, with the CAI INS providing periodic measurements to correct the solution. This approach was chosen due to the known performance of a navigation grade INS over a wide range of system dynamics - there will never be an outage of the navigation grade measurements. A concern with this approach was the use of the navigation measurements for mechanization at all times. The white noise errors of the navigation grade INS are not estimated and corrected like the bias and scale factor errors. Because of this, these errors will lead to what is commonly referred to as velocity and angular random walk errors. The previous framework minimized these errors by mechanizing off of the CAI-INS measurements whenever they were available. Because of the use of the Pinson error model in this framework, one set of measurements must be used. This is because the Pinson error model is estimating errors in a single INS, and switching back and forth between INS as in Framework 1 would mean the errors were from two different INS. To examine the effect of the velocity and angular random walk errors, a set of measurements were corrupted with only white noise. The results of this sample trajectory is shown in Fig 3.7. It can be seen in the figure that the error due to white noise only in the navigation grade system is on the order of tens of meters. Considering the total system error is on the order of a nautical mile, this framework should still correct the majority of the error. For comparison, Fig 3.8 shows the error due to white noise only for a tactical grade system. These errors are on the order of thousands of meters. Again, these errors would not be corrected, so using at least a navigation grade INS for Framework 2 is a minimum requirement.
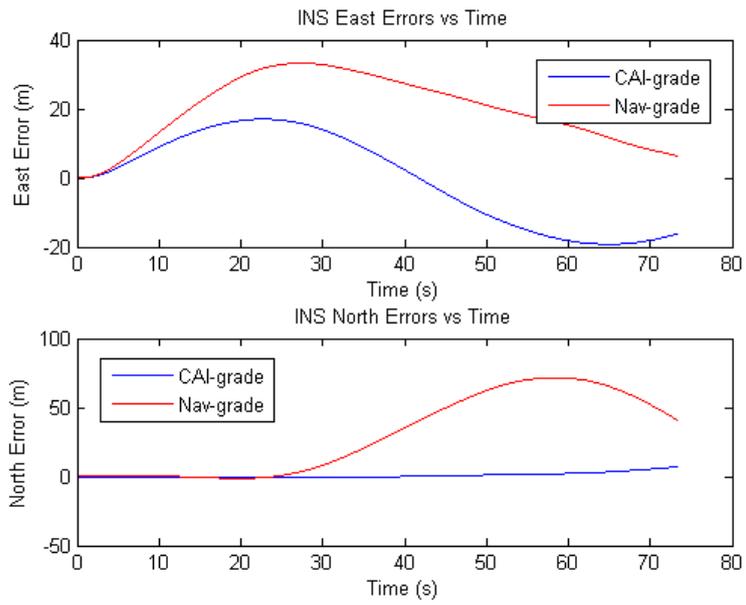
Figure 3.7:   Comparison of Navigation Grade and CAI Grade INS System Showing North Error Due to Measurement White Noise Only on a Sample Trajectory
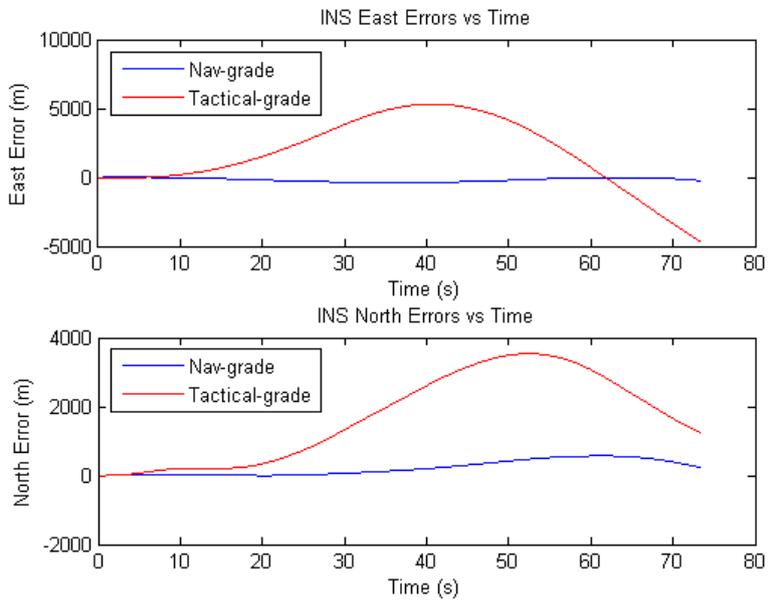

Figure 3.8:   Comparison of Navigation Grade and CAI Grade INS System Showing East Error Due to Measurement White Noise Only On A Sample Trajectory

The states of the implemented Kalman filter are given in Table 3.2. The $\mathbf{F}$ matrix is given in Eq 3.22. The Pinson error model is a matrix of equations that models the dynamics of errors in a strapdown INS [6].

$$\mathbf{F} = \begin{bmatrix} Pinson & \mathbf{A} & \mathbf{C} & \mathbf{D} & \mathbf{E} & 0 \\ 0 & \mathbf{B} & 0 & 0 & 0 & 0 \\ 0 & 0 & 0 & 0 & 0 & 0 \end{bmatrix}_{41x41} \qquad (3.22)$$

$$\mathbf{P} = \begin{bmatrix} 0 & 0 & -\frac{v_N}{R_{Earth}^2} & \frac{1}{R_{Earth}} & 0 \\ \frac{v_E \tan(L)}{R_{Earth}\cos(L)} & 0 & \frac{-v_E}{R_{Earth}^2\cos(L)} & 0 & \frac{1}{R_{Earth}\cos(L)} \\ 0 & 0 & -k1 & 0 & 0 \\ -v_E(2\Omega\cos(L) + \frac{v_E}{R_{Earth}\cos^2(L)}) & 0 & \frac{v_E^2\tan(L)-v_N v_D}{R_{Earth}^2} & \frac{v_D}{R_{Earth}} & -2(\Omega\sin(L) + \frac{v_E\tan(L)}{R_{Earth}} \\ 2\Omega(v_N\cos(L) - v_D\sin(L)) + \frac{v_N v_E}{R_{Earth}\cos^2(L)} & 0 & -v_E\frac{v_N\tan(L)+v_D}{R_{Earth}^2} & 2\Omega\sin(L) + \frac{v_E\tan(L)}{R_{Earth}} & \frac{v_N\tan(L)+v_D}{R_{Earth}} \\ 2\Omega v_E\sin(L) & 0 & \frac{v_N^2+v_E^2}{R_{Earth}^2}+k2 & -2\frac{v_N}{R_{Earth}} & -2(\Omega\cos(L) - \frac{v_E}{R_{Earth}} \\ -\Omega\sin(L) & 0 & -\frac{v_E^2}{R_{Earth}^2} & 0 & \frac{1}{R_{Earth}} \\ 0 & 0 & \frac{v_N}{R_{Earth}^2} & \frac{-1}{R_{Earth}} & 0 \\ -\Omega\cos(L) - \frac{v_E}{R_{Earth}\cos^2(L)} & 0 & \frac{v_E\tan(L)}{R_{Earth}^2} & 0 & \frac{-\tan(L)}{R_{Earth}} \\ 0 & 0 & 0 & 0 & 0 \\ 0 & 0 & k3 & 0 & 0 \end{bmatrix} \cdots$$

$$(3.23)$$

$$\cdots \begin{bmatrix} 0 & 0 & 0 & 0 & 0 & 0 \\ 0 & 0 & 0 & 0 & 0 & 0 \\ -1 & 0 & 0 & 0 & k1 & 0 \\ \frac{v_N}{R_{Earth}} & 0 & -f_{NED}(3) & f_{NED}(2) & 0 & 0 \\ 2\Omega\cos(L) + \frac{v_E}{R_{Earth}} & f_{NED}(3) & 0 & -f_{NED}(1) & 0 & 0 \\ 0 & -f_{NED}(2) & f_{NED}(1) & 0 & -k2 & 1 \\ 0 & 0 & -\Omega\sin(L) - \frac{v_E\tan(L)}{R_{Earth}} & \frac{v_N}{R_{Earth}} & 0 & 0 \\ 0 & \Omega\sin(L) + \frac{v_E\tan(L)}{R_{Earth}} & 0 & \Omega\cos(L) + \frac{v_E}{R_{Earth}} & 0 & 0 \\ 0 & \frac{-v_N}{R_{Earth}} & -\Omega\cos(L) - \frac{v_E}{R_{Earth}} & 0 & 0 & 0 \\ 0 & 0 & 0 & 0 & \frac{-1}{Baro_T} & 0 \\ 0 & 0 & 0 & 0 & -k3 & 0 \end{bmatrix} \quad (3.24)$$

The $\mathbf{A}$ matrix relates how the bias errors flow back into the velocity and attitude error states. Note that a direction cosine matrix is needed because bias errors are in the

Table 3.2:   Dual INS Filter States

Filter States	Description
δL	Error in Latitude
$\delta\lambda$	Error in Longitude
δh	Error in Height
δV_N	Error in North Velocity
δV_E	Error in East Velocity
δV_D	Error in Down Velocity
$\delta\alpha$	North Tilt Error
$\delta\beta$	East Tilt Error
$\delta\gamma$	Down Tilt Error
δh_a	Aiding Altitude Error
$\delta\hat{a}$	Vertical Acceleration Error
$\mathbf{b}_a$	X,Y, and Z Accelerometer Bias
$\mathbf{b}_\theta$	X,Y, and Z Gyro Bias
$\mathbf{SF}_a$	X,Y, and Z Accelerometer Linear Scale Factor
$\mathbf{SF}_\theta$	X,Y, and Z Gyro Linear Scale Factor
$\mathbf{NSF}_a$	X,Y, and Z Accelerometer Non Linear Scale Factor
$\mathbf{NSF}_\theta$	X,Y, and Z Gyro Non Linear Scale Factor
$\mathbf{ASF}_a$	X,Y, and Z Accelerometer Asymmetric Scale Factor
$\mathbf{ASF}_\theta$	X,Y, and Z Gyro Asymmetric Scale Factor
$\mathbf{\Delta V}_{true}$	X,Y, and Z True X-Accelerometer ΔV
$\mathbf{\Delta\theta}_{true}$	X,Y, and Z True X-Gyro $\Delta\theta$

body frame, not the navigation frame. The $\frac{1}{dt}$ term is needed because the bias states are an estimate of the biases in the ΔV and $\Delta \theta$ measurements. These measurements are just changes in velocity and angular rate (not changes in velocity and angular rate over time) and must be divided by time to be made into average accelerations before they can be integrated into velocity and attitude. The **A** matrix is given by

$$
\mathbf{A} = \frac{1}{dt} \cdot \begin{bmatrix} 0 & 0 \\ \mathbf{C}_n^b & 0 \\ 0 & \mathbf{C}_n^b \\ 0 & 0 \end{bmatrix}_{11x6}
\tag{3.25}
$$

The **B** matrix describes the dynamics of the time-correlated biases as first order Gauss Markov processes with time constants equal to τ. The **B** matrix is given by

$$
\mathbf{B} = \begin{bmatrix} -1/\tau_{ax} & 0 & 0 & \cdots \\ 0 & -1/\tau_{ay} & 0 & \cdots \\ \vdots & \vdots & \ddots & \vdots \\ 0 & \cdots & -1/\tau_{gy} & 0 \\ 0 & \cdots & 0 & -1/\tau_{gz} \end{bmatrix}_{6x6}
\tag{3.26}
$$

The **C**, **D**, and **E** matrices describe how the linear scale factor, non linear scale factor, and asymmetric scale factor errors relate to the velocity and attitude states. Again, these terms must be divided by time so the changes in velocity and attitude become average accelerations over time. The elements of the direction cosine matrix which converts from the body frame to the navigation frame must be included as well. The **C**, **D**, and **E** matrices are given by

$$
\mathbf{C} = \frac{1}{dt} \cdot \begin{bmatrix} 0_{3x3} & 0_{3x3} \\ C1_{3x3} & 0_{3x3} \\ 0_{3x3} & C2_{3x3} \\ 0_{2x2} & 0_{2x3} \end{bmatrix}_{11x6}
\tag{3.27}
$$

39

$$\mathbf{C1} = \begin{bmatrix} \mathbf{C}_n^b(1,1)\Delta V_x & \mathbf{C}_n^b(1,2)\Delta V_y & \mathbf{C}_n^b(1,3)\Delta V_z \\ \mathbf{C}_n^b(2,1)\Delta V_x & \mathbf{C}_n^b(2,2)\Delta V_y & \mathbf{C}_n^b(2,3)\Delta V_z \\ \mathbf{C}_n^b(3,1)\Delta V_x & \mathbf{C}_n^b(3,2)\Delta V_y & \mathbf{C}_n^b(3,3)\Delta V_z \end{bmatrix} \tag{3.28}$$

$$\mathbf{C2} = \begin{bmatrix} \mathbf{C}_n^b(1,1)\Delta\theta_x & \mathbf{C}_n^b(1,2)\Delta\theta_y & \mathbf{C}_n^b(1,3)\Delta\theta_z \\ \mathbf{C}_n^b(2,1)\Delta\theta_x & \mathbf{C}_n^b(2,2)\Delta\theta_y & \mathbf{C}_n^b(2,3)\Delta\theta_z \\ \mathbf{C}_n^b(3,1)\Delta\theta_x & \mathbf{C}_n^b(3,2)\Delta\theta_y & \mathbf{C}_n^b(3,3)\Delta\theta_z \end{bmatrix} \tag{3.29}$$

$$\mathbf{D} = \frac{1}{dt} \cdot \begin{bmatrix} 0_{3x3} & 0_{3x3} \\ D1_{3x3} & 0_{3x3} \\ 0_{3x3} & D2_{3x3} \\ 0_{2x2} & 0_{2x3} \end{bmatrix}_{11x6} \tag{3.30}$$

$$\mathbf{D1} = \begin{bmatrix} \mathbf{C}_n^b(1,1)\Delta V_x^2 & \mathbf{C}_n^b(1,2)\Delta V_y^2 & \mathbf{C}_n^b(1,3)\Delta V_z^2 \\ \mathbf{C}_n^b(2,1)\Delta V_x^2 & \mathbf{C}_n^b(2,2)\Delta V_y^2 & \mathbf{C}_n^b(2,3)\Delta V_z^2 \\ \mathbf{C}_n^b(3,1)\Delta V_x^2 & \mathbf{C}_n^b(3,2)\Delta V_y^2 & \mathbf{C}_n^b(3,3)\Delta V_z^2 \end{bmatrix} \tag{3.31}$$

$$\mathbf{D2} = \begin{bmatrix} \mathbf{C}_n^b(1,1)\Delta\theta_n^2 & \mathbf{C}_n^b(1,2)\Delta\theta_e^2 & \mathbf{C}_n^b(1,3)\Delta\theta_d^2 \\ \mathbf{C}_n^b(2,1)\Delta\theta_n^2 & \mathbf{C}_n^b(2,2)\Delta\theta_e^2 & \mathbf{C}_n^b(2,3)\Delta\theta_d^2 \\ \mathbf{C}_n^b(3,1)\Delta\theta_n^2 & \mathbf{C}_n^b(3,2)\Delta\theta_e^2 & \mathbf{C}_n^b(3,3)\Delta\theta_d^2 \end{bmatrix} \tag{3.32}$$

$$\mathbf{E} = \frac{1}{dt} \cdot \begin{bmatrix} 0_{3x3} & 0_{3x3} \\ E1_{3x3} & 0_{3x3} \\ 0_{3x3} & E2_{3x3} \\ 0_{2x2} & 0_{2x3} \end{bmatrix}_{11x6} \tag{3.33}$$

$$\mathbf{E1} = \begin{bmatrix} \mathbf{C}_n^b(1,1)|\Delta V_x| & \mathbf{C}_n^b(1,2)|\Delta V_y| & \mathbf{C}_n^b(1,3)|\Delta V_z| \\ \mathbf{C}_n^b(2,1)|\Delta V_x| & \mathbf{C}_n^b(2,2)|\Delta V_y| & \mathbf{C}_n^b(2,3)|\Delta V_z| \\ \mathbf{C}_n^b(3,1)|\Delta V_x| & \mathbf{C}_n^b(3,2)|\Delta V_y| & \mathbf{C}_n^b(3,3)|\Delta V_z| \end{bmatrix} \tag{3.34}$$

$$\mathbf{E2} = \begin{bmatrix} \mathbf{C}_n^b(1,1)|\Delta\theta_n| & \mathbf{C}_n^b(1,2)|\Delta\theta_e| & \mathbf{C}_n^b(1,3)|\Delta\theta_d| \\ \mathbf{C}_n^b(2,1)|\Delta\theta_n| & \mathbf{C}_n^b(2,2)|\Delta\theta_e| & \mathbf{C}_n^b(2,3)|\Delta\theta_d| \\ \mathbf{C}_n^b(3,1)|\Delta\theta_n| & \mathbf{C}_n^b(3,2)|\Delta\theta_e| & \mathbf{C}_n^b(3,3)|\Delta\theta_d| \end{bmatrix} \tag{3.35}$$

The noise vector $\mathbf{w}$ contains 18 noise sources which account for what is commonly referred to as velocity or angular random walk as well as the driving noises for the accelerometer and gyroscope biases. They also include the tuning noises for the ΔV_{true} and $\Delta\theta_{true}$ states. The noise vector is given by

$$\mathbf{w} = \begin{bmatrix} \mathbf{w}_{accel}^{vrw} \\ \mathbf{w}_{gyro}^{arw} \\ \mathbf{w}_{accel}^{bias} \\ \mathbf{w}_{gyro}^{bias} \\ \mathbf{w}_{accel}^{tuning} \\ \mathbf{w}_{gyro}^{tuning} \end{bmatrix}_{18x1} \tag{3.36}$$

Where

$\mathbf{w}_{accel}^{vrw} = $ x,y, and z velocity random walk noise

$\mathbf{w}_{gyro}^{arw} = $ x,y, and z angular random walk noise

$\mathbf{w}_{accel}^{bias} = $ x,y, and z accel time-correlated bias driving noise

$\mathbf{w}_{gyro}^{bias} = $ x,y, and z gyro time-correlated bias driving noise

$\mathbf{w}_{accel}^{tuning} = $ Accel True ΔV Tuning Noise

$\mathbf{w}_{gyro}^{tuning} = $ Gyro True $\Delta\theta$ Tuning Noise

The $\mathbf{G}$ matrix is needed to relate noises in the body frame to noises in the navigation frame. The only noises that must be converted are the velocity and angular random

Table 3.3:   Conventional and CAI INS Parameter Values [5]

Conventional Accelerometer White Noise Variance	$(5 \times 10^{-5} m/s^2/\sqrt{Hz})^2$
Conventional Gyroscope White Noise Variance	$(6 \times 10^{-2} deg/h/\sqrt{Hz})^2$
CAI Accelerometer White Noise Variance	$(3 \times 10^{-8} m/s^2/\sqrt{Hz})^2$
CAI Gyroscope White Noise Variance	$(1.2 \times 10^{-4} deg/h/\sqrt{Hz})^2$
Conventional Accelerometer Bias Variance	$(2 \times 10^{-4} m/s^2)^2$
Conventional Gyroscope Bias Variance	$(3 \times 10^{-3} deg/h)^2$
Conventional Accelerometer Scale Factors (1 σ value)	300ppm
Conventional Gyroscope Scale Factors (1 σ value)	300ppm

walk noises. The **G** matrix is given by

$$
\mathbf{G} = \begin{bmatrix} \mathbf{A} & 0 & 0 \\ 0 & \mathbf{I} & 0 \\ 0 & 0 & 0 \\ 0 & 0 & \mathbf{I} \end{bmatrix}_{41x18}
\tag{3.37}
$$

$$
\mathbf{A} = \begin{bmatrix} 0 & 0 \\ \mathbf{C}_n^b & 0 \\ 0 & \mathbf{C}_n^b \\ 0 & 0 \end{bmatrix}_{11x6}
\tag{3.38}
$$

The measurement model and measurement matrix **z** are the same as Framework 1.
The H matrix is different, but the sub matrices **SF**, **NSF**, and **ASF** are the same as
Framework 1.

$$
\mathbf{H} = \begin{bmatrix} 0 & 0 & 0 & 0 & 0 & \mathbf{I} \\ 0 & \mathbf{I} & \mathbf{SF} & \mathbf{NSF} & \mathbf{ASF} & \mathbf{I} \end{bmatrix}_{12x41}
\tag{3.39}
$$

Using the **F**, **G**, and **H** matrices, a Kalman filter can be implemented. The navigation
grade INS inputs drive the mechanization equations. The mechanization equations are
used to provide nominal values for calculating the time varying **F** and **H** matrices.
The error state solutions from the Kalman Filter are added to the mechanization
equation outputs to provide a corrected navigation solution. The parameters used for
the white noise, biases, and scale factors are given in Table 3.3.
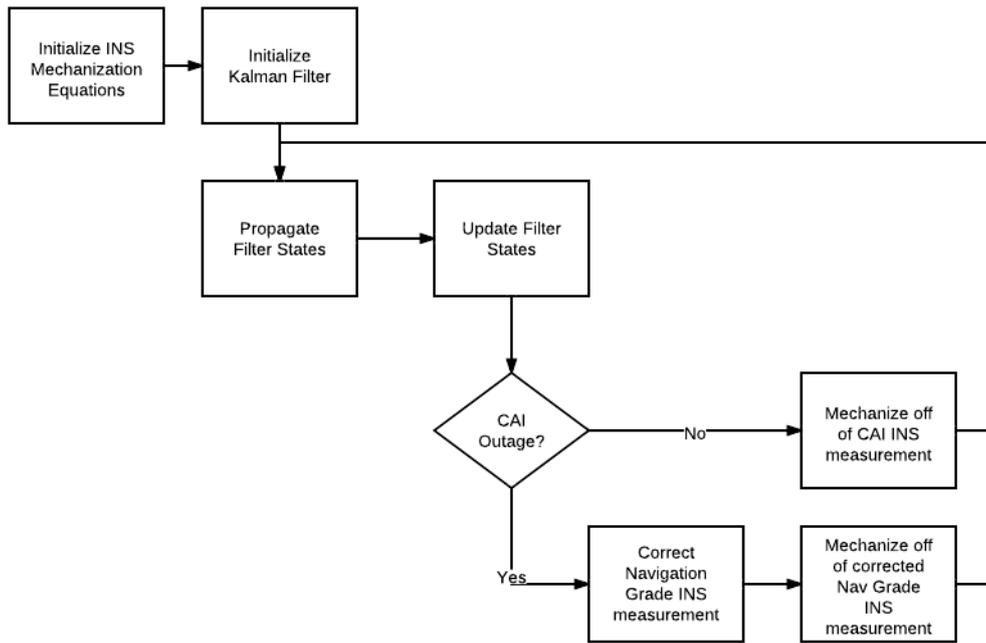
Figure 3.9:   Framework 1 Dual INS Simulation Flow Chart

3.5   Algorithm Implementation for Dual INS Framework

The algorithms for implementing the Dual-INS simulation are presented in this section. A large part of the simulation consists of creating the measurements needed by the Kalman Filter. This process in done in two steps. A MATLAB m-file creates the true measurements from ECEF data as explained in the beginning of Chapter 3. Second, a MATLAB m-file corrupts these measurements according to the two separate models explained in Chapter 2. Finally, the simulation is run in a final MATLAB m-file. The Framework 1 flowchart for this simulation is shown in Fig 3.9. The Framework 2 flowchart is shown in Fig 3.10.

3.6   Converting from IMU specifications to code parameters

IMU's are described by specifications such as velocity random walk. These specifications can be used to derive the parameters needed when simulating an IMU in software. The software in this simulation consists of measurements given in the

43
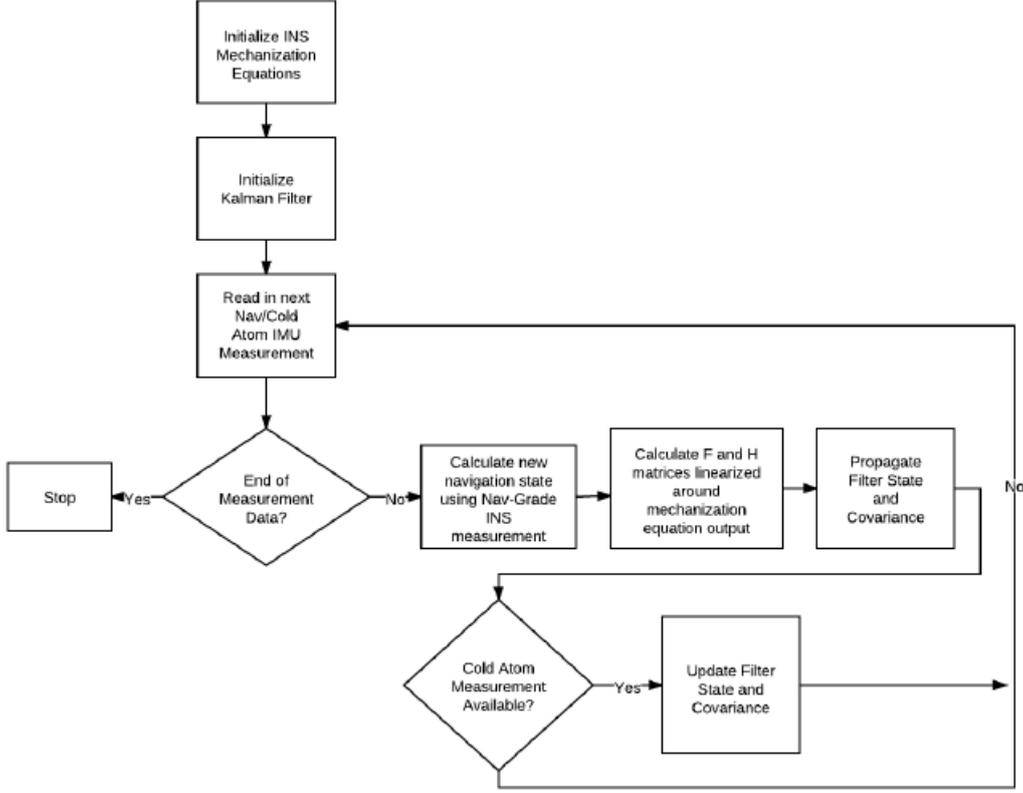
Figure 3.10:   Framework 2 Dual INS Simulation Flow Chart

form of ΔV's. These are not the same as sampled accelerations. Data sheets for IMU systems often give parameters as sampled acceleration. The process of converting between these types of measurements is given in this section. The velocity random walk specification often given in IMU data sheets can be used to calculate the white noise strength of accelerometer ΔV measurements. The white noise process of an accelerometer sensor is described by

$$E[w_{\Delta V_x}(t_j)w_{\Delta V_x}(t_k)] = \sigma^2_{w\Delta V_x}\delta_{jk} \qquad (3.40)$$

The following equation relates VRW to the variance of the white noise samples.

$$(VRW)^2 \Delta t = \sigma^2_{w\Delta V_x} \qquad (3.41)$$

44

The measurement bias is described as a first order Gauss Markov process which is expressed by the following differential equation.

$$\dot{b}_{\Delta V_x} = -\frac{1}{T_{accel}} b_{\Delta V_x} + w_{\Delta V bias_x} \tag{3.42}$$

The noise term $w_{\Delta V bias_x}$ is defined by

$$E[w_{\Delta V bias_x}(t) w_{\Delta V bias_x}(t + \tau)] = Q_{b\Delta V} \delta(\tau) \tag{3.43}$$

In code, this bias will be created by driving white noise through a system. The strength of this driving white noise must be calculated from the given bias 1 sigma value often found in specifications. The following equation relates the bias variance given in specifications to driving white noise strength.

$$Q_{b\Delta V} = \frac{2(\Delta t)\sigma_{accel}^2}{T_{accel}} \tag{3.44}$$

3.7 GPS-CAI Integration

The integration of GPS with CAI INS was done using a Kalman Filter. The approach chosen was that of a classic loosely coupled INS-GPS like that found in [9]. The integration framework can be seen in Fig 3.11. The states of the filter are given in Table 4.6. The F matrix was the Pinson error model augmented with accelerometer and gyroscope bias states.

$$\mathbf{F} = \begin{bmatrix} Pinson & 0 & 0 \\ 0 & b_a & 0 \\ 0 & 0 & b_g \end{bmatrix}_{18x18} \tag{3.45}$$

The noise vector $\mathbf{w}$ contains 12 noise sources which account for what is commonly referred to as velocity or angular random walk as well as the driving noises for the

45
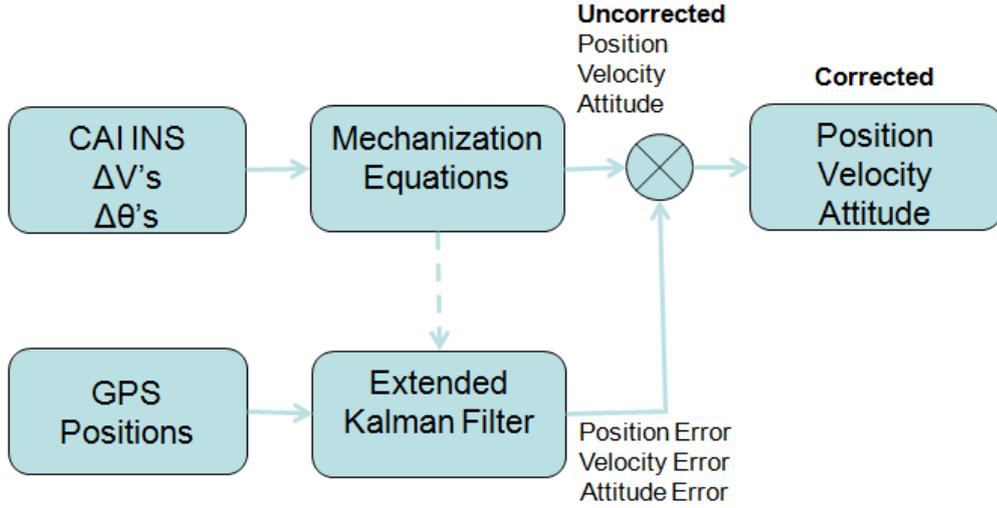
Figure 3.11:   GPS-CAI INS Integration Framework

accelerometer and gyroscope biases. The noise vector is given by

$$
\mathbf{w} = \begin{bmatrix} \mathbf{w}_{accel}^{vrw} \\ \mathbf{w}_{gyro}^{arw} \\ \mathbf{w}_{accel}^{bias} \\ \mathbf{w}_{gyro}^{bias} \end{bmatrix}_{12x1}
\tag{3.46}
$$

Where

$\mathbf{w}_{accel}^{vrw}$ = x,y, and z velocity random walk noise

$\mathbf{w}_{gyro}^{arw}$ = x,y, and z angular random walk noise

$\mathbf{w}_{accel}^{bias}$ = x,y, and z accel time-correlated bias driving noise

$\mathbf{w}_{gyro}^{bias}$ = x,y, and z gyro time-correlated bias driving noise

The G matrix is given by

$$
\mathbf{G} = \begin{bmatrix} \mathbf{A} & 0 \\ 0 & \mathbf{I} \end{bmatrix}_{17x12}
\tag{3.47}
$$

Table 3.4:   GPS-CAI INS Filter States

Filter States	Description
δL	Error in Latitude
$\delta\lambda$	Error in Longitude
δh	Error in Height
δV_N	Error in North Velocity
δV_E	Error in East Velocity
δV_D	Error in Down Velocity
$\delta\alpha$	North Tilt Error
$\delta\beta$	East Tilt Error
$\delta\gamma$	Down Tilt Error
δh_a	Aiding Altitude Error
$\delta\hat{a}$	Vertical Acceleration Error
b_a	X,Y, and Z Accelerometer Bias
b_θ	X,Y, and Z Gyro Bias

$$\mathbf{A} = \begin{bmatrix} 0 & 0 \\ \mathbf{C}_n^b & 0 \\ 0 & \mathbf{C}_n^b \\ 0 & 0 \end{bmatrix}_{11x6} \tag{3.48}$$

The measurement model is given by the following equations

$$Latitude_{GPS} = Latitude_{INS} + \delta Latitude \tag{3.49}$$

$$Longitude_{GPS} = Longitude_{INS} + \delta Latitude \tag{3.50}$$

$$\tag{3.51}$$

The GPS position is converted to a latitude and longitude and then used as the measurement in the Kalman Filter.

$$\mathbf{z} = \begin{bmatrix} Latitude_{GPS} - Latitude_{INS} \\ Longitude_{GPS} - Longitude_{INS} \end{bmatrix} \tag{3.52}$$

47

The above equations lead to the following $\mathbf{H}$ matrix.

$$\mathbf{H} = \begin{bmatrix} 1 & 0_{1x16} & 0 \\ 0 & 1 & 0_{1x16} \end{bmatrix}_{2x18} \tag{3.53}$$

3.8   Algorithm Implementation for GPS-CAI INS Framework

The GPS measurements are created by running the uncorrupted ΔV and $\Delta\theta$ measurements through the INS mechanization equations. The resulting true latitudes, longitudes, and heights are saved for use in generating the measurements. This is done in the same MATLAB m-file that corrupts the measurements for use in the dual-INS framework. The flowchart for this simulation is shown in Fig 3.12
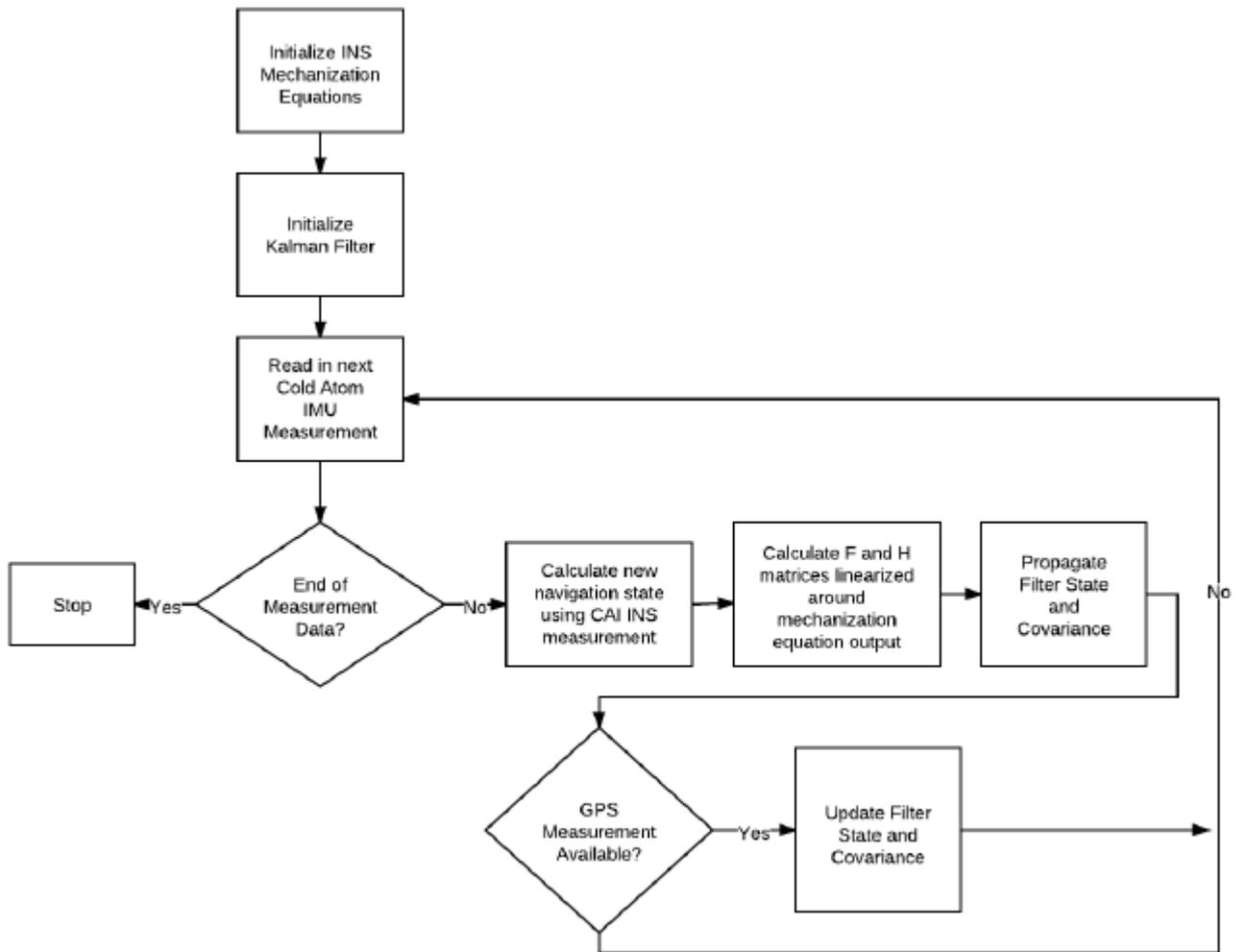
Figure 3.12:   GPS-CAI INS Simulation Flow Chart

IV. Results

4.1 Test Environments

4.1.1 Dual-INS Test Environments. The Dual-INS frameworks were simulated in various test environments. As explained in Chapter 2, CAI sensors may not operate in high dynamic environments. Because the CAI INS is still under development, two key testing parameters were created to cover a range of possible performance levels. The first is the CAI white noise errors. As explained in the CAI INS error model, the errors are modeled by a single additive white noise. This white noise is varied in the simulation to simulate the various levels that could be encountered in a CAI system. The second parameter is called the g cut-off, which is the maximum acceleration possible before creating a CAI outage. The algorithm calculates the acceleration as each measurement comes in. If it is above a certain threshold, a CAI outage is created. Table 4.1 shows what percent of the flight the CAI INS failed. Fig 4.1-4.3 shows CAI measurement availability for a 3, 5, and 7 g-cutoff. By varying these two parameters, a tradespace can be analyzed. True values used for error calculations were created by passing the uncorrupted ΔV and $\Delta \theta$ measurements through the mechanization equations. Note that the CAI-grade and nav-grade measurements were created by corrupting these true measurements.

An additional method for creating CAI INS outages was tested. This method used periodic outages of the CAI INS instead of g-induced outages. This allows for more general analysis to be conducted on the filter framework. The g-induced outages are more realistic, yet also very specific to the created flight trajectory. The observable errors in the navigation grade INS are hidden beneath white noise. These white noise errors are reduced with the square root of time as CAI INS measurements are taken. Because of this, CAI INS measurements cannot be taken at long intervals. If a measurement was taken every 5 seconds the bias would be indistinguishable from

Table 4.1:   Dual INS CAI Outage Times for Tested G Cutoffs

| G-cutoff	3 g's	5 g's	7 g's
Percent of flight with CAI outage	27%	15%	7%
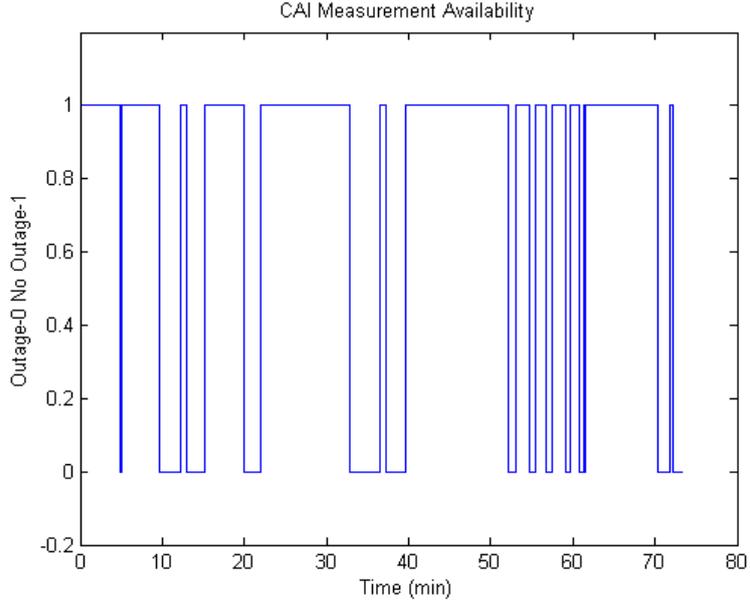
Figure 4.1: Dual INS Example of a 3 G-Dependent CAI Measurement Availability

the white noise. Fig 4.4 shows the filter's bias estimate using CAI INS measurements every 5 seconds as opposed to every time step. It can be seen the filter does not track the bias error accurately, which would lead to poor navigation performance. The periodic outages are instead modeled as square waves with various periods as well as duty cycles. For example, an outage may occur every 10 seconds and last for 3 seconds. Fig 4.5 shows an example of test case with a measurement period of 10 minutes and duty cycles of 50, 70, and 90 percent. This allows the time of continuous measurement needed to calibrate the navigation grade INS.

4.1.2 GPS-CAI INS Test Environments. The GPS-CAI INS test environment was designed to simulate GPS outages. A GPS fix gives absolute location, so the performance of the system while continually receiving GPS updates is not of importance. Instead, the performance of the system subjected to various length GPS outages will be analyzed. The simulation for the GPS-CAI integration varied one parameter. This parameter will be called measurement frequency and is simply the number of GPS measurements per unit of time.

51
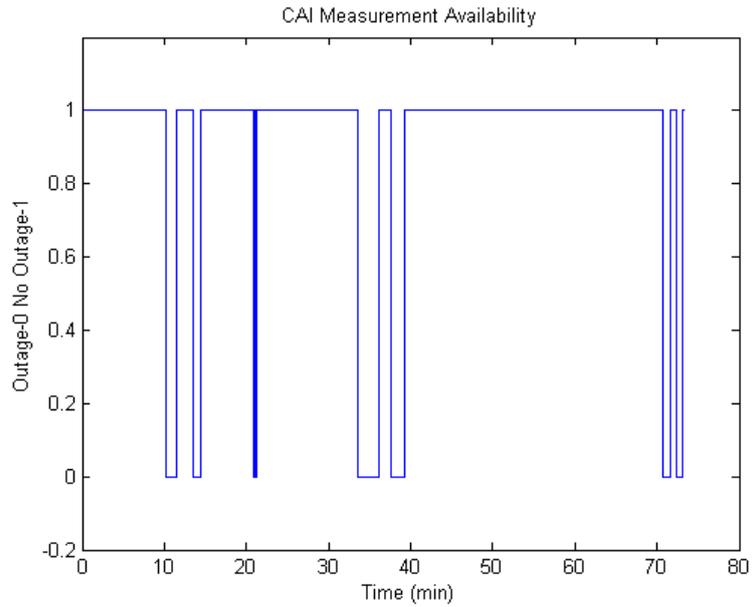
Figure 4.2:   Dual INS Example of 5 G-Dependent CAI Measurement Availability

The accelerometer measurements that were used in the simulation are given in Fig 4.6-4.8. These plots are useful for understanding the vehicle dynamics. The Y and Z accelerometers measured greater variations in acceleration over time than the X accelerometer. The X-accelerometer was aligned along the length of the aircraft and would be especially sensitive to such maneuvers as speeding up and slowing down. These types of maneuvers are not as frequent in the flight trajectory.
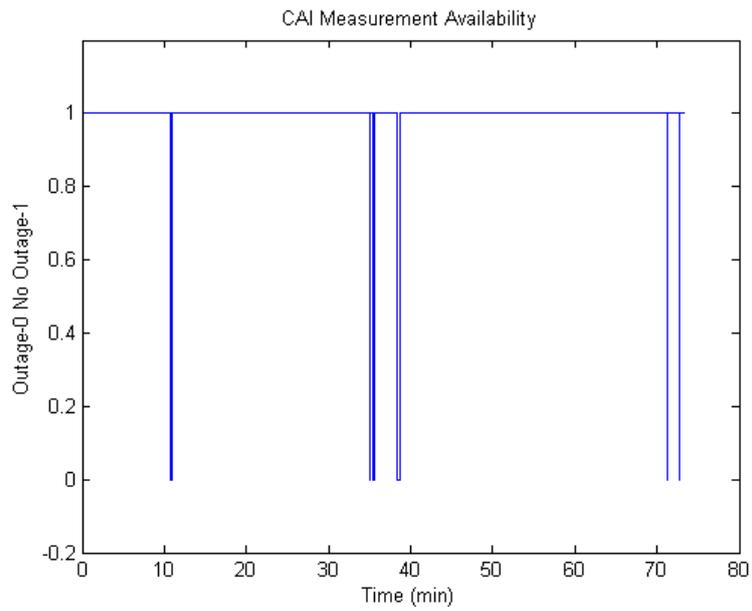
Figure 4.3:   Dual INS Example of a 7 G-Dependent CAI Measurement Availability
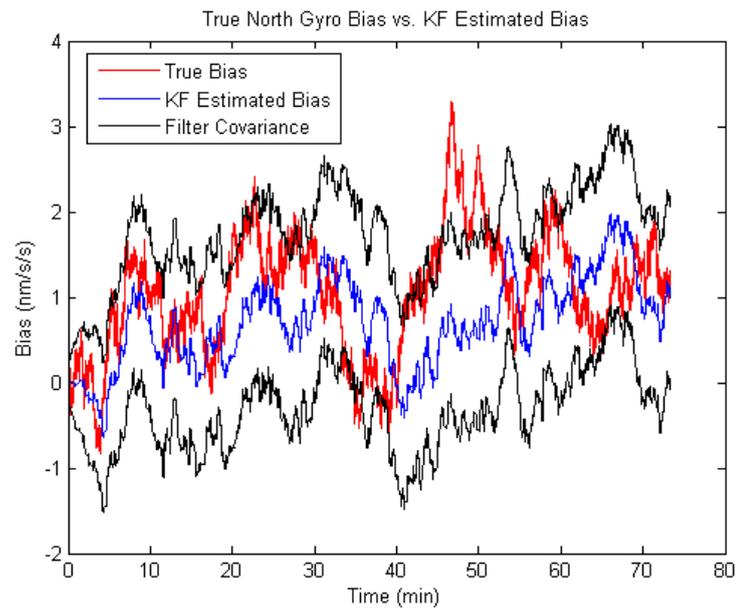
Figure 4.4:   Dual INS Insufficient Measurement Rate Example Showing Failed Bias Estimate
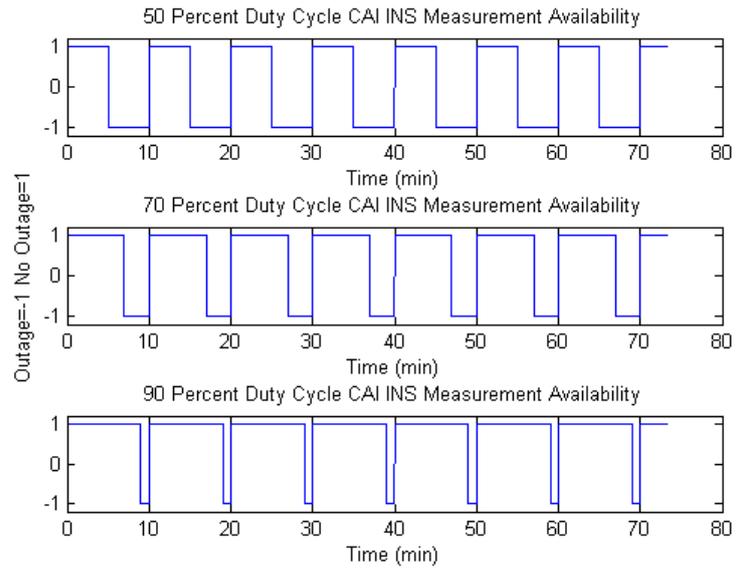
Figure 4.5:   Periodic CAI INS Measurement Availability, Period=10 Minutes, Duty Cycles=50,70,90 Percent
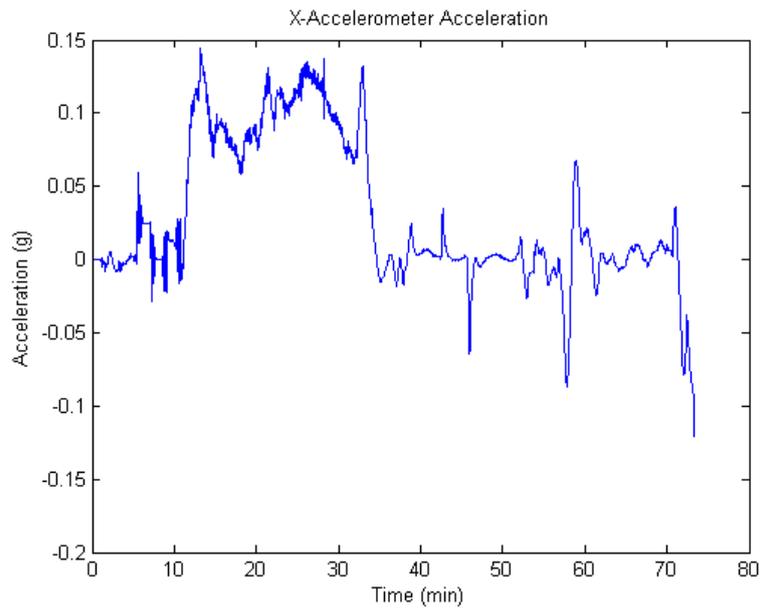
Figure 4.6:   Dual INS Sample Trajectory X-Accelerometer Measured Acceleration vs. Time

54
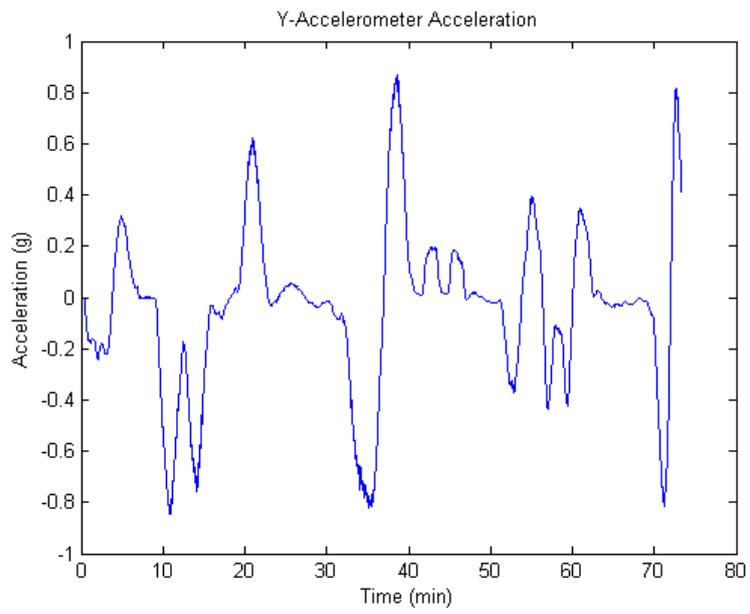
Figure 4.7:   Dual INS Sample Trajectory Y-Accelerometer Measured Acceleration vs. Time
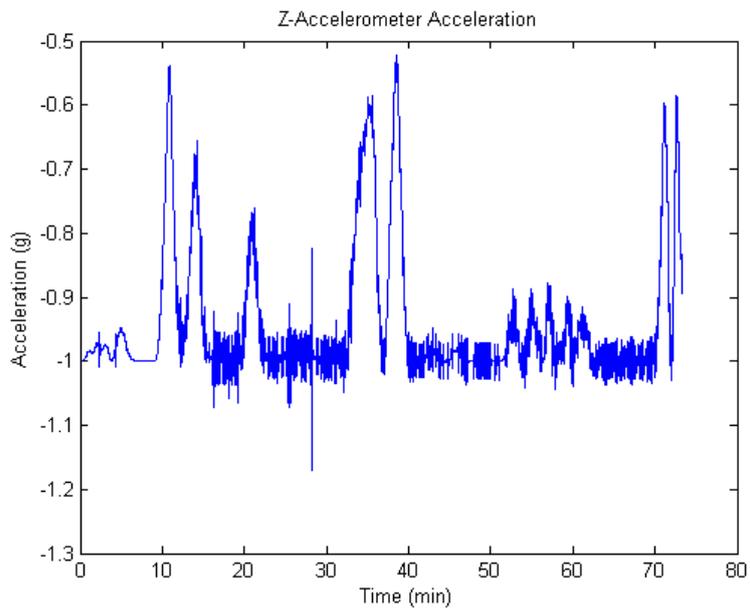
Figure 4.8:   Dual INS Sample Trajectory Z-Accelerometer Measured Acceleration vs. Time

4.2   Dual INS Filter Performance

The following sections present the results of the different dual INS filters implemented. The performance of the different approaches are presented first, followed by a comparison to the other filter frameworks. Framework 2 had superior performance when subjected to realistic outages, and therefore has the most complete analysis, and will be presented first. The reasons for Framework 2's superior performance under realistic outages will explained when comparing the filter frameworks.

4.2.1   Framework 2 Results.   Framework 2 always mechanized off the navigation grade measurements. The errors in the navigation grade measurements were continuously estimated with a Kalman Filter and propagated though the Pinson error model to be corrected at the position domain level (as opposed to correcting the measurements as Framework 1 did). The use of the Pinson error model will allow measurements coming into the filter to make corrections to the systems attitude, velocity, and position. A drawback of Framework 2 is that the more accurate CAI INS measurements are never used for mechanization - they are only used to correct the navigation grade INS errors. This means that any errors the filter is not estimating, such as the navigation grade white noise, will not be corrected. This was not a large concern due to the low contribution of the velocity and angular random walk errors to the overall system error. Fig 4.9 shows a sample run of the error of a navigation grade system due to white noise only. It can be seen the error is on the order of 50 meters per hour, while the total system error is on the order of a nautical mile per hour. This indicates that mechanizing off of the navigation grade measurements is an acceptable approach.

Values for the white noise level of a CAI system are given in Table 4.2. In this simulation, these values are referred to as the nominal values. These values, along with a g-cutoff of 3 g's, will be used to demonstrate the success of Framework 2. Fig 4.10 and 4.11 show the east and north errors of the corrected vs. uncorrected solutions for a sample run. It can be seen from the plots that the errors are dramatically

56
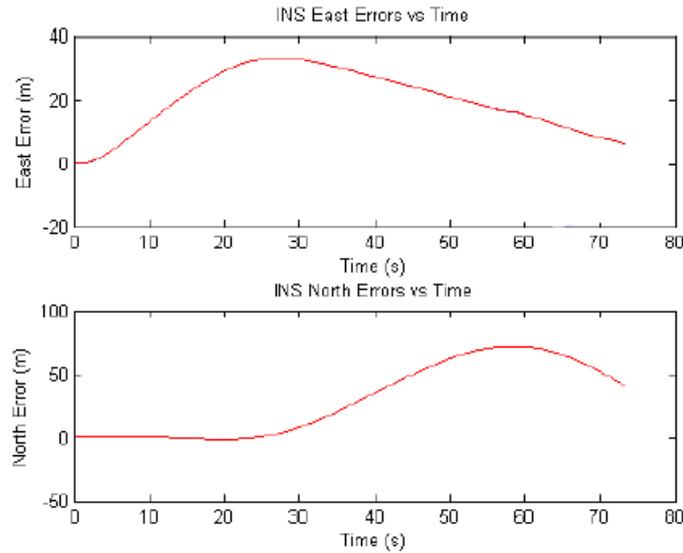
Figure 4.9: Sample Run Showing East Error Due to VRW and ARW Only for a Navigation Grade System

reduced when aided with the CAI system. The errors of both the aided and unaided solutions are seen to be driven primarily by the Shuler cycle. In the aided solution, small jumps may be seen in the error that coincide with the return of CAI availability. An expanded view of these jumps can be seen in Fig 4.12. Such jumps are desired since they indicate that the filter is able to use new measurements to correct past errors, rather than just ensuring the current solution is more accurate from that time forward. This may seem normal when thinking about the problem in the same way as GPS aiding, but it must be pointed out that the measurements are not in the position domain. When an INS system receives a GPS measurement, it is receiving a position domain estimate, so the position solution is corrected. When the dual-INS system receives a measurement after an outage, it is only getting a more accurate acceleration back. Previous errors have already been integrated twice into position errors. The correction in the position domain shows the filter's use of the correlation between various states, demonstrating the usefulness of the chosen approach to dual INS integration.

57

Table 4.2:   Conventional and CAI INS Parameter Values [5]

| Conventional Accelerometer White Noise Variance | $(5 \times 10^{-5} m/s^2/\sqrt{Hz})^2$ |
Conventional Gyroscope White Noise Variance	$(6 \times 10^{-2} deg/h/\sqrt{Hz})^2$
CAI Accelerometer White Noise Variance	$(3 \times 10^{-8} m/s^2/\sqrt{Hz})^2$
CAI Gyroscope White Noise Variance	$(1.2 \times 10^{-4} deg/h/\sqrt{Hz})^2$
Conventional Accelerometer Bias Variance	$(2 \times 10^{-4} m/s^2)^2$
Conventional Gyroscope Bias Variance	$(3 \times 10^{-3} deg/h)^2$
Conventional Accelerometer Scale Factors (1 σ value)	300ppm
Conventional Gyroscope Scale Factors (1 σ value)	300ppm

Figure 4.10:   Dual INS Framework 1 North Corrected vs. Uncorrected Error For Single Run, 3 G Cutoff, Nominal Case

4.2.1.1   Monte Carlo Results.   Using the nominal parameter values given in the previous section, a Monte Carlo analysis was done. The same simulation was run fifty times. Fig 4.13-4.14 show all fifty runs on a single plot along with the filter predicted standard deviation.   The true ΔV and $\Delta \theta$ values were corrupted differently for all 50 runs. Fig 4.15-4.16 shows the mean error over the fifty runs, as well as the filter predicted and actual standard deviations. The errors appear to be converging on zero-mean as Monte Carlo runs increase. With 50 runs they still drift slowly over time. More Monte Carlo runs would be needed to confirm that the errors are indeed zero mean. The North and East channel predicted and actual standard deviations match up accurately.

58
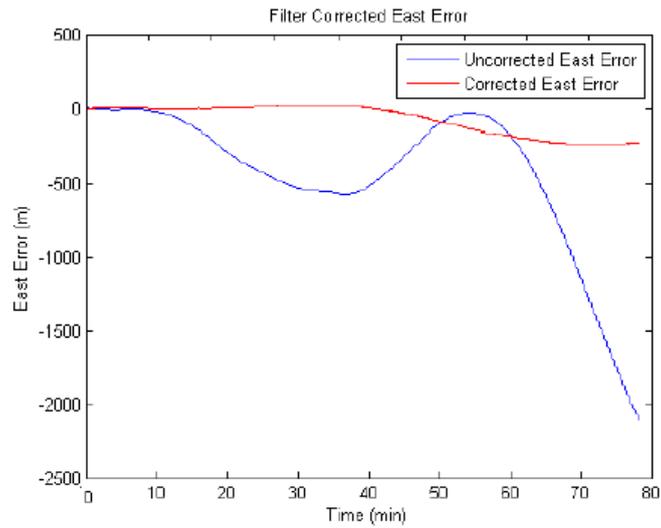
Figure 4.11:   Dual INS Framework 1 East Corrected vs. Uncorrected Error For Single Run, 3 G Cutoff, Nominal Case

For comparison, Fig 4.17 and 4.18 show the uncorrected navigation grade INS mean and standard deviation. As Monte Carlo runs are increased the position errors appear to be converging on zero mean. Again, more Monte Carlo runs would be needed to confirm this. As expected the standard deviations are much higher in the uncorrected case.
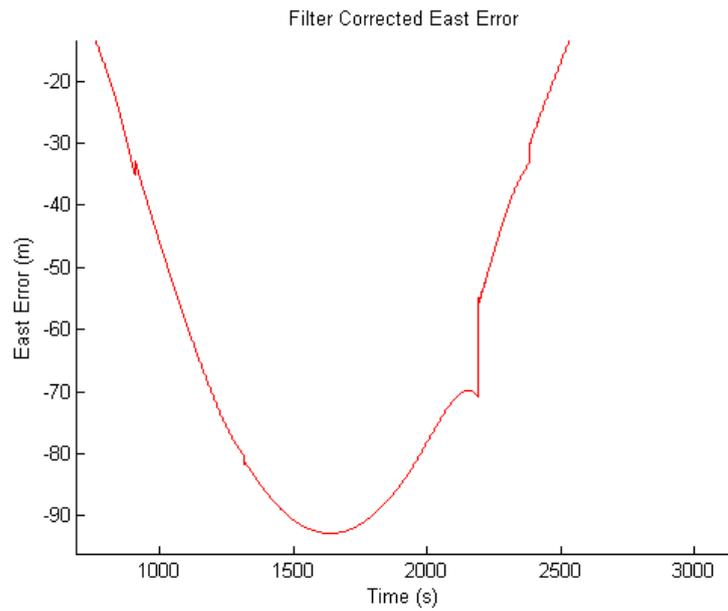
Figure 4.12:   Dual INS Framework 1 East Corrected Solution Example of Improvement Jumps Coinciding with Returning CAI Measurements, 3 G Cutoff, Nominal Case
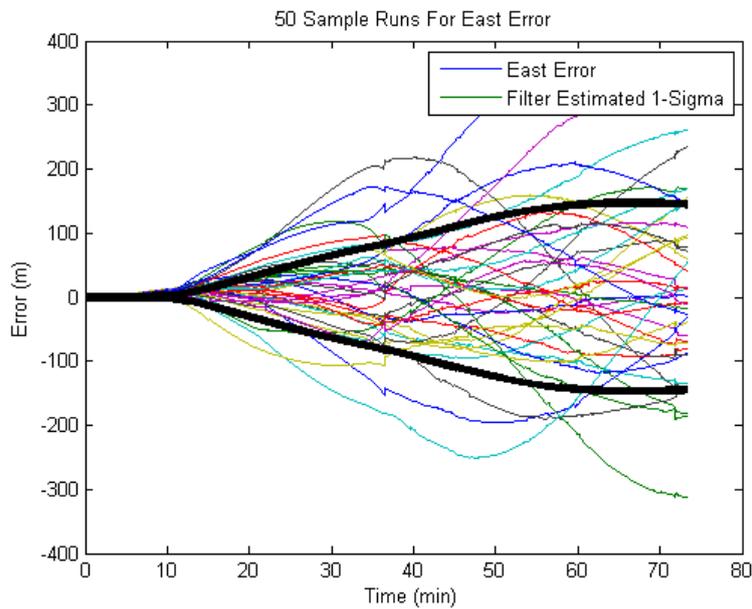
Figure 4.13:   Dual INS Framework 1 Monte Carlo East Error VS Time for All Runs, 3 G Cutoff, Nominal Case

60
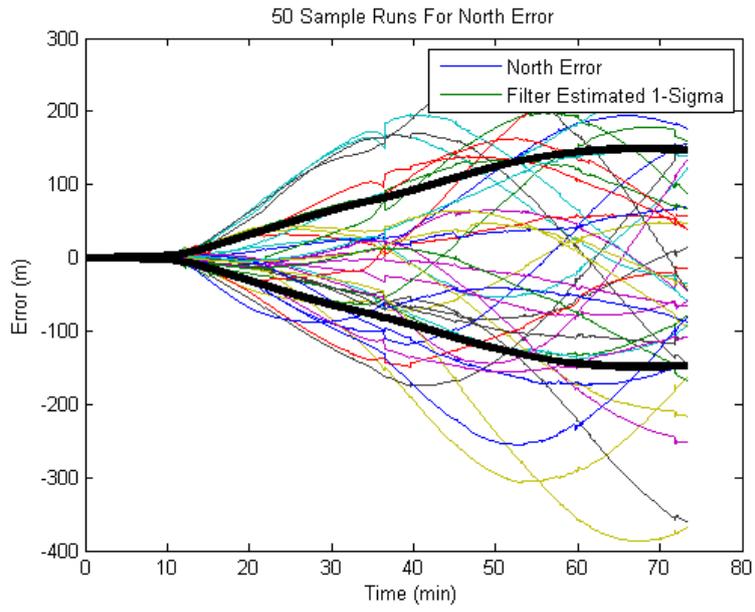
Figure 4.14:   Dual INS Framework 1 Monte Carlo Uncorrected North Error VS
Time for All Runs, 3 G Cutoff, Nominal Case
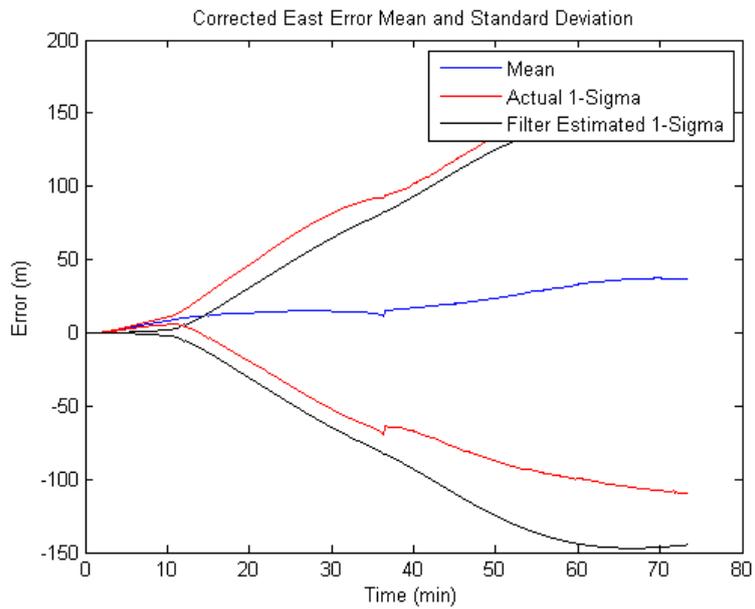
Figure 4.15:   Dual INS Framework 1 Monte Carlo Filter Corrected East Error vs.
Time, 3 G Cutoff, Nominal Case

61
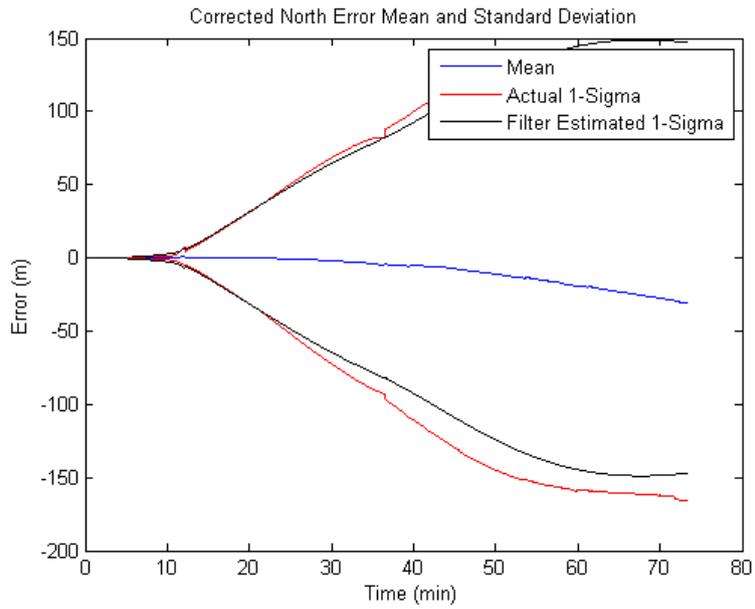
Figure 4.16: Dual INS Framework 1 Monte Carlo Filter Corrected North Error vs. Time, 3 G Cutoff, Nominal Case
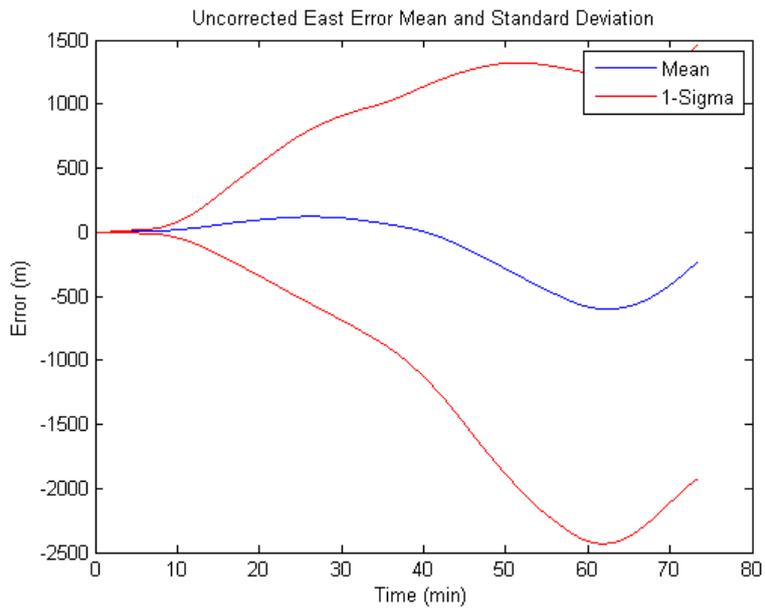
Figure 4.17: Dual INS Framework 1 Monte Carlo Uncorrected East Error VS Time, 3 G Cutoff, Nominal Case
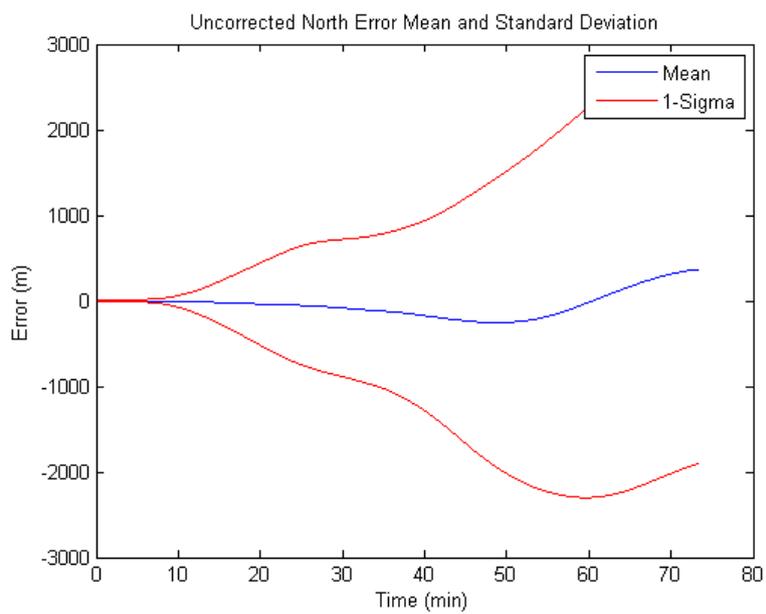
Figure 4.18:   Dual INS Framework 1 Monte Carlo Uncorrected North Error VS Time, 3 G Cutoff, Nominal Case

The RMS errors in both the north and east directions were calculated over the fifty runs giving RMS value at each point in time. A RMS value was also calculated over time characterizing the north and east error with a single RMS value. Fig 4.19 show the north and east RMS errors vs. time for the corrected and uncorrected solutions. Fig 4.20 shows the north and east RMS errors vs. time for the corrected vs. basic integration. These plots show consistently growing error, which is to be expected for a RMS value. The RMS values are useful for characterizing the performance of the system over time. The jumps in the position solution when obtaining CAI measurements after an outage are more prominent in these plots, further demonstrating the successful performance of the filter.

4.2.1.2 Individual Error Plots. 24 separate error sources are being corrected in the filter. For ease of presentation, only a few will be shown. All 24 of these errors are propagated though the Pinson Error Model to predict the error in the navigation solution. Fig 4.21 shows the filter's estimate of the navigation grade x-axis accelerometer bias. It can easily be seen where CAI outages are taking place during the flight. The periods of growing covariances in Fig 4.21 indicate an outage is taking place. Because of the filter's knowledge of the time constant of the bias, the estimate of the bias remains accurate for the duration of the outages. Fig 4.22 shows the down gyroscope scale factor. It can be seen that outages do not appear to affect the estimate of this scale factor. This is a desirable filter characteristic. Once the filter correctly tracks a scale factor error, this error will be corrected for the remainder of the flight. In this simulation the scale factors are modeled as constants, which is why the filter keeps an accurate estimate even during outages. Realistically, the scale factors could vary with time, but for a short flight this is a reasonable assumption. Fig 4.23 shows the asymmetric north gyro scale factor errors. Again, this estimate is not affected by outages. It can be seen that the filter does a good job estimating these values. There are small errors throughout which will continually be integrated twice into position errors. The filter was not able to track all errors, however. Not
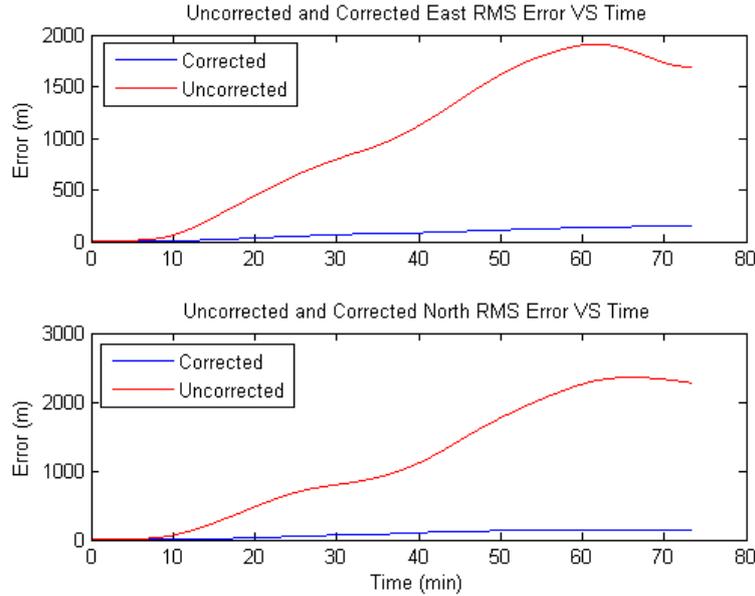
Figure 4.19:   Dual INS Framework 1 Monte Carlo Corrected and Uncorrected East and North RMS Error VS Time, 3 G Cutoff, Nominal Case

all modes of the filter were excited enough to gain observability on all filter states. Errors such as nonlinear scale factors would gain observability better in a higher-g turn. Observability on the scale factor errors is related to the variation in the accelerometer measurements. This is why the down scale factors tend to be tracked more accurately than the north or east scale factors. The variation in acceleration in the z accelerometer is greater than the x or y accelerometers, as shown in Section 4.1. A benefit of the chosen approach is the performance while coasting through outages. Even with no measurements available the filter is still able to estimate the errors fairly well.

The results are now summarized in Table 4.3. As stated previously, the first metric of success is the percent improvement over the uncorrected solution. The second metric of success is the percent improvement over a basic integration that simply uses CAI measurements when they are available, and performs no optimal estimation. It can be seen in from the results that the filter makes large improvements with respect to both measures of success. The corrected horizontal error is on the

65
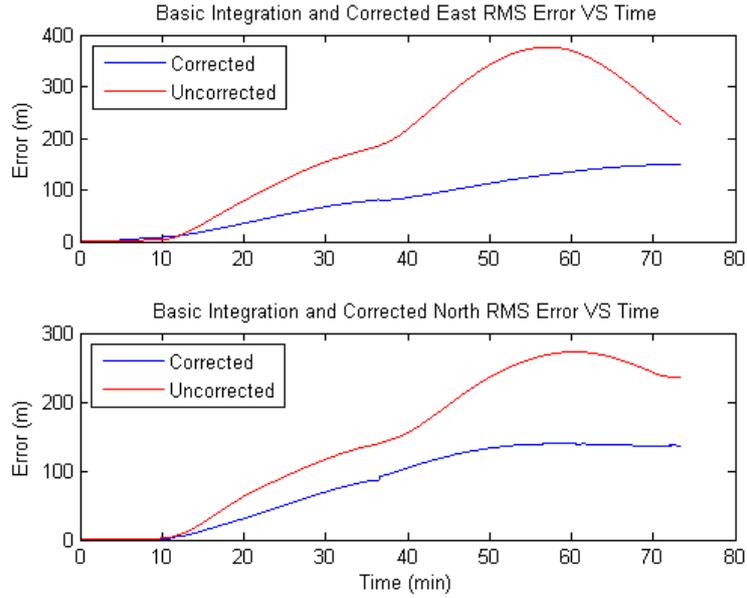
Figure 4.20:   Dual INS Framework 1 Monte Carlo Corrected and Simplistic Integration East and North RMS Error VS Time, 3 G Cutoff, Nominal Case

order of 100 meters. This was done using 3-g induced outages, which made the CAI INS unavailable 27 percent of the time. With full measurement availability the CAI INS is predicted to be a 5 meter per hour system. 100 meter per hour performance appears reasonable with outages of the system for almost one third of the flight. The test case of 3-g induced outages was considered a worst case performance, giving results still significantly better than current navigation grade systems.
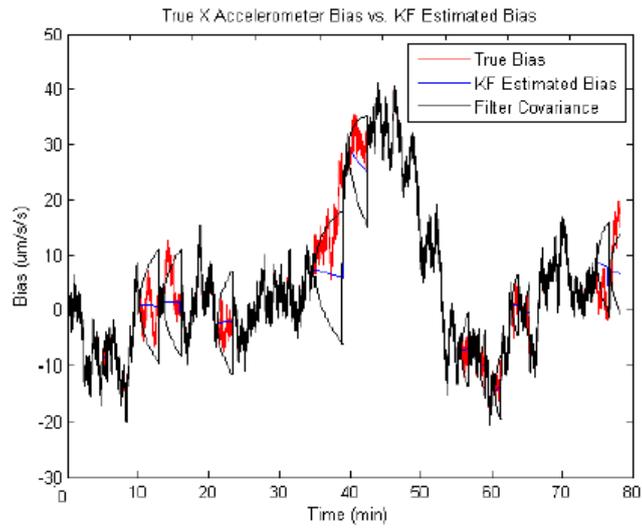
Figure 4.21:   Dual INS Framework 1 Filter X-Accelerometer Bias Estimate Example for Single Run, 3 G Cutoff, Nominal Case
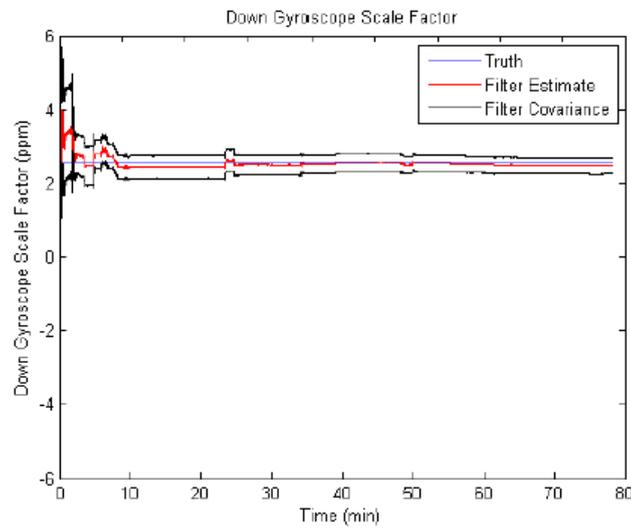
Figure 4.22:   Dual INS Framework 1 Filter Down Gyroscope SF Estimate Example for Single Run, 3 G Cutoff, Nominal Case
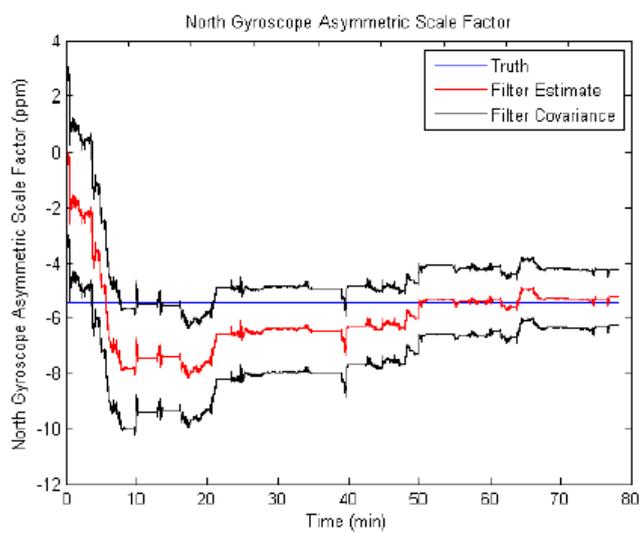
Figure 4.23:   Dual INS Framework 1 Filter North Gyroscope Assymetric SF Estimate Example for Single Run, 3 G Cutoff, Nominal Case

Table 4.3:   Dual INS Framework 1 RMS Errors and Percent Improvements, 3 G
Cutoff, Nominal Case

	East RMS Error (m)	North RMS Error (m)	Horizontal RMS Error (m)
Uncorrected Error (Metric 1)	1215	1428	1871
Basic Integration Error (Metric 2)	231	173	289
Corrected Error	92 meters	97	134
Improvement over uncorrected (% improvement)	1320%	1472%	1396%
Improvement over basic (% improvement)	251 %	178%	216 %

Table 4.4:   Dual INS Framework 1 Tradespace Monte Carlo DRMS Errors VS CAI
White Noise and G-Cutoff

Nominal Value ×	3-g	5-g	7-g
1	135	72	33
100	140	81	32
500	132	103	77
1000	165	134	93

4.2.1.3   Trade-space Results.   A large number of simulations were conducted to capture the possible range of performances for a CAI-INS integrated with a conventional INS. These results are presented in the form of DRMS error. The tradespace consists of two parameters. The first is a multiplier of the nominal white noise value. This is to simulate changing the accuracy of the CAI system. The second parameter is the g-cutoff of the CAI system. Table 4.4 shows the DRMS errors across the tradespace. It was discovered in the simulations that the white noise of the CAI system must be increased greatly before it starts having a noticeable effect on the filter results. Decreasing the white noise levels below the nominal case was found to yield negligible improvement for the filter as well.

69

4.2.2   Dual INS Framework 1 Results.   Framework 1 switched between using CAI INS measurements and corrected navigation grade measurements in the mechanization equations. A Kalman Filter continuously estimated the error of the navigation grade measurements in order to correct them in the event of an outage. Framework 1 was simulated for various test cases. Monte Carlo results of these simulations are shown in Table 4.5. A metric of performance was needed to evaluate the performance of each framework. The chosen metric of performance is the percent improvement over what is called the dual INS basic integration. The dual INS basic integration is a simple integration of the two INS that does not use any optimal estimation. It simply uses the CAI INS measurements when they are available, and uses the navigation grade INS measurements when the CAI INS is not available. It is similar to Framework 1, except in the event of an outage the navigation grade INS measurements are not corrected with the estimated errors of the navigation grade system. Each framework will be compared to the performance of this basic integration. The actual numerical performance of the filter framework is not the primary concern of this analysis. A simple model of the CAI INS was used and the extent of the dynamic performance limitations being addressed will not be fully understood until these systems, still under development, are fully tested. The research is primarily concerned with the performance of the different integration approaches relative to each other, as well as trends in the data seen under the various test cases.

The first test case is the no-outage test case, shown in the first line of Table 4.5. This test case measures how well the framework performs when the CAI INS measurements are always available. For Framework 1 this test case is trivial, as the CAI INS is used the entire flight. This test case is useful for later comparing to Framework 2.

The next test cases were the periodic outage test cases. These test cases used square waves with a period of 600 seconds and varying duty cycles, where a 1 corresponds to measurement availability and a -1 corresponds to a CAI INS outage. In this way the amount of time each system was subjected to CAI outages was easily

70
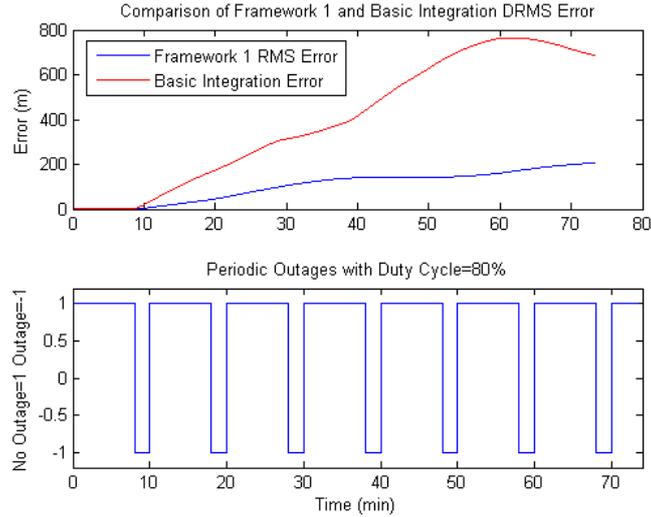
Figure 4.24:   Dual INS Periodic Outages with Measurement Period of 600 Seconds and Duty Cycle of 80%

controlled and the performance with these outage times evaluated. The duty cycles chosen were based off the outage times they create. A duty cycle of 97 percent creates 20 second outages while a duty cycle of 80 percent creates 2 minute outages. An example of these periodic outages can be seen in Fig 4.24, and results are given in Table 4.5.

The next test cases were the g-induced outages. These outages are created when the aircraft acceleration exceeds a set threshold. These outages are more realistic than the periodic outages, as this is how an outage would actually be created, as explained in the Background section. A drawback is these outages are very specific to the flight trajectory created for this simulation. An example of a g-induced outage can be seen in Fig 4.25.

It can be seen from the results that Framework 1 had the greatest factor of improvement over the basic integration when there was short CAI INS outages, such as the 5g induced outages. This shows the usefulness of estimating the navigation grade INS errors. Even short outages will cause errors that oscillate and grow according to the dynamics of the Schuler cycle. With longer outages the corrected solution also begins to have noticeable Schuler cycle oscillations, decreasing the factor

71
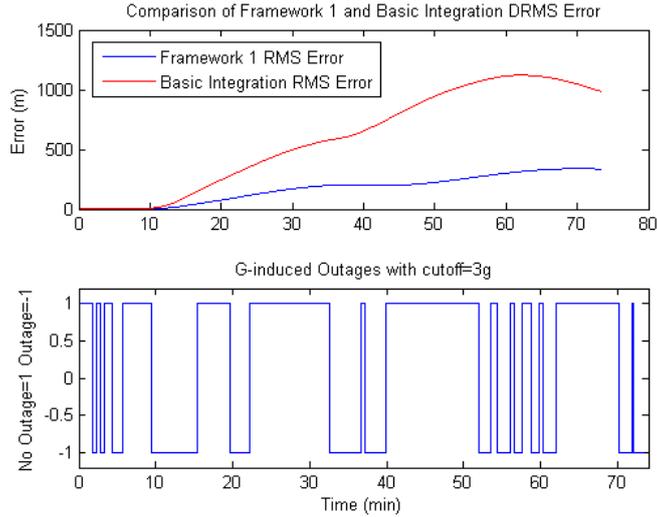
Figure 4.25:   Dual INS G-Induced Outages with G Threshold of 3G's

Table 4.5:   Dual INS Framework 1 MC DRMS Error Under Various Test Cases

Test Case	Basic Integration	Framework 1	Factor of Improvement
No Outages	2 m	2 m	0 x
97% Duty Cycle	77 m	12 m	6.4 x
80% Duty Cycle	483 m	124 m	3.9 x
3g Induced Outages	718 m	205 m	3.5 x
5g Induced Outages	540 m	133 m	4.1 x

of improvement. The test case with the longest outages was the 3-g induced outage case. This test case had outages for 27 percent of the time. The error from the basic integration, which still uses CAI INS whenever it can, grows to 718 meters. That error is decreased by more than 500 meters by estimating the navigation grade errors during outages. Note that altitude errors are omitted because they are bounded by the barometer aiding that occurs in the mechanization equations and therefore have a negligible effect on overall system error.

72
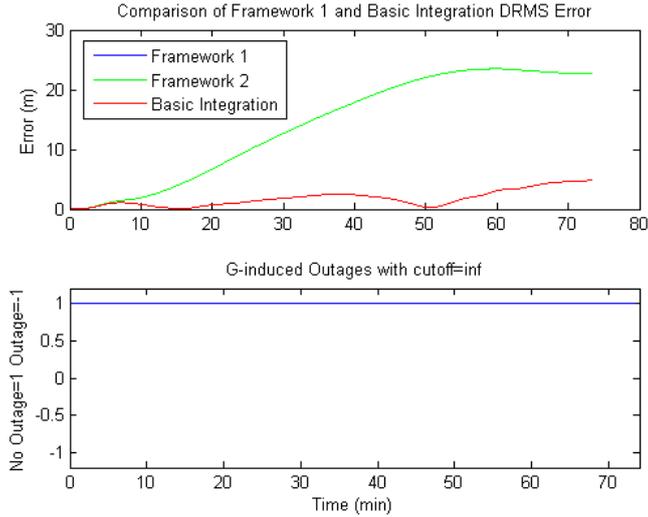
Figure 4.26: Dual INS Comparison of Framework 1 and 2 Errors with No CAI INS Outages (Framework 1 and Basic Integration Error are Identical)

4.2.3 Dual INS Framework 1 and 2 Comparisons. The performance of Framework 2 is compared to the basic integration error as well as the Framework 1 errors for all of the previously described test cases. The Monte Carlo results of these simulations are in Table 4.6. Fig 4.26 shows the results of the two filter frameworks when there are no CAI INS outages. As expected, Framework 1 performs better than Framework 2, and is exactly the same as the basic integration. Framework 1 has no velocity and angular random walk errors when there are no CAI INS outages, because the navigation grade INS is never used. Framework 2 always mechanizes off of the CAI INS so VRW and ARW errors accumulate for the duration of the flight. Fig 4.27 shows a comparison of the Framework 1 and Framework 2 performances for a periodic outage with a duty cycle of 97 percent. It can be seen that Framework 1 performs better than Framework 2 in this case. The outage times with a 97 percent duty cycle are very short - around 20 seconds. With these small outages correcting the measurements at the measurement level gives better results. Fig 4.28 shows the results of the 80 percent duty cycle case. In this case Framework 2 performs better. This is likely due to the benefits of using the Pinson error model. A duty cycle of 80 percent corresponds to outage times of two minutes. When outage times are this long there is much to

73
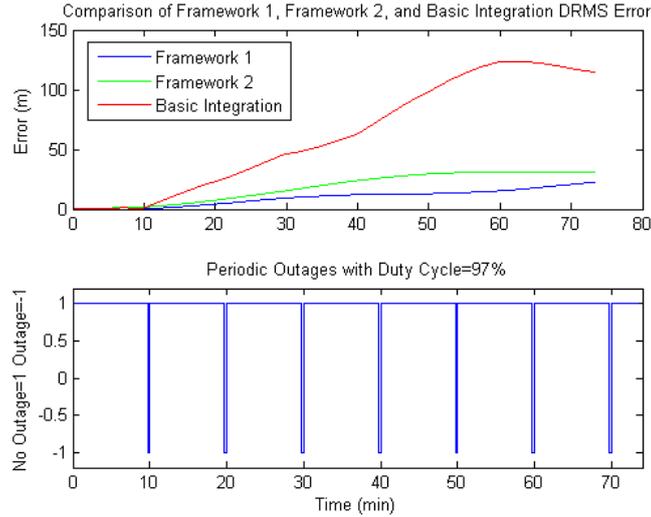
Figure 4.27:   Dual INS Periodic Outages with Measurement Period of 600 Seconds and Duty Cycle of 97%

be gained by using the Pinson error model. When CAI INS measurements return, the Kalman Filter is able to make corrections to the position, velocity, and attitude states. The bias changes enough over the two minute outage that when the filter gets a measurement back it is able to adjust these states accordingly to reflect what the true bias actually was. This is possible because of the cross correlation between the bias states and the Pinson error states. An additional test case was run to find out at what point Framework 1 and 2 have the same performance for the periodic outages. This was determined to occur when the duty cycle of the outages is 93% which corresponds to outage times of about 40 seconds. A comparison of the filter performances when using the g-induced outages is given in Fig 4.29. It can be seen from the data that Framework 2 performs better in the g-induced outages. This is because of the long outages in these cases. The performance in these cases is important, because these types of outages are what a CAI INS with dynamic limitations could encounter. Again it can be seen that Framework 2 performs much better than Framework 1.

When comparing the first two filter frameworks it can be seen there is a tradeoff between outage times and which framework performs better. When the outage times are very short, the first framework has better performance. There could be several

74
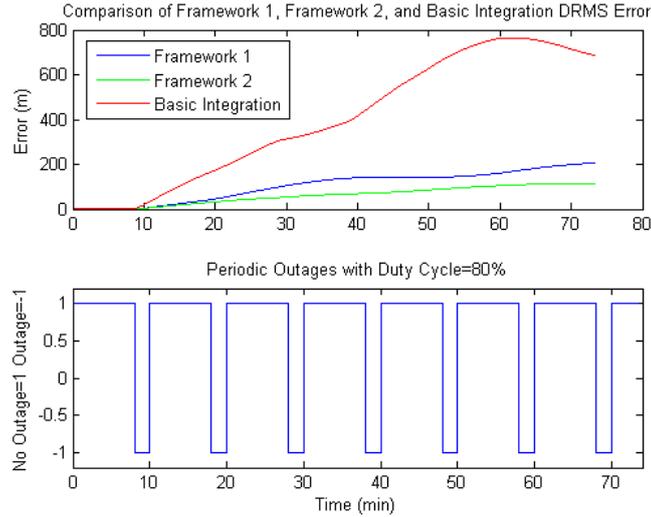
Figure 4.28:   Dual INS Periodic Outages with Measurement Period of 600 Seconds and Duty Cycle of 80%

Table 4.6:   Dual INS Framework 1 and 2 MC DRMS Errors Under Various Test Cases

Test Case	Basic Integration	Framework 1	Framework 2
No Outages	2 m	2 m	16 m
97% Duty Cycle	77 m	12 m	22 m
93% Duty Cycle	179 m	26 m	27 m
80% Duty Cycle	483 m	124 m	72 m
3g Induced Outages	718 m	205 m	111 m
5g Induced Outages	540 m	133 m	69 m

reasons for this improved performance. It is possible that when the outage times are short the dominant error comes from velocity and angular random walk errors. These errors are more prominent in Framework 2, because the mechanization is done using the navigation grade measurements, whereas Framework 1 uses the CAI INS measurements whenever they are available. It was shown that the VRW and ARW errors are small compared to the error from the biases. This would explain why only during short outages, when bias errors don't have time to accumulate, that Framework 1 shows the best performance. This idea will be tested with the design of a third framework. This framework will attempt to reduce the VRW and ARW

75
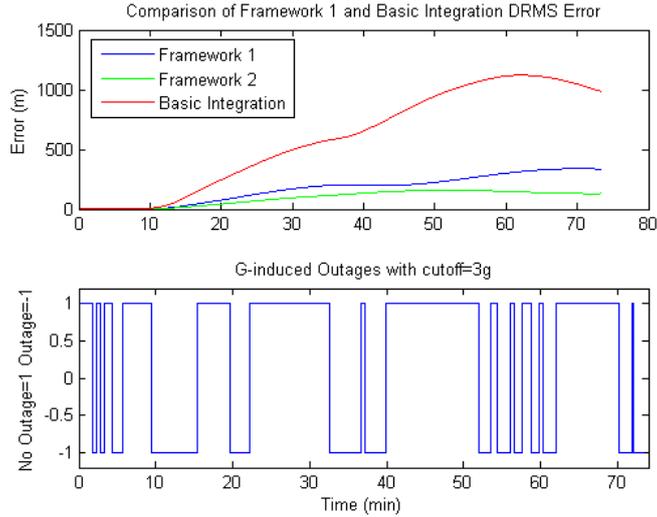
Figure 4.29: Dual INS G-Induced Outages with G Cutoff of 3G's

errors. The goal will be a framework that always performs better than Framework 1 and Framework 2, regardless of outage times.

4.3 Dual INS Framework 3 Design

The third filter framework made corrections at the measurement level and the position level. It has been shown that using the Pinson error model is beneficial. A drawback of the second framework, however, is that it mechanizes off of the navigation grade INS measurements at all times. This allows velocity and angular random walk noise to accumulate. The Pinson error model is estimating the errors of the navigation grade system only, so it is problematic to switch back and forth between the CAI INS and the navigation grade INS, as Framework 1 does. If this was done, the Pinson error model would become invalid - the INS that it is attempting to model is now a hybrid of two systems. Instead, an additional filter is implemented which attempts to reduce the white noise of the navigation grade measurements prior to mechanization. This is done to reduce the velocity and angular random walk noise from the navigation grade measurements. The third framework is simply the second framework with this additional step. A moving average filter was used to accomplish

Table 4.7:   Comparison of All Three Dual INS Filter Frameworks

Test Case	Framework 1	Framework 2	Framework 3
97% Duty Cycle	12 m	22 m	23 m
80% Duty Cycle	124 m	72 m	71 m
Time Correlated Bias Only	124	78	78 m
3g Induced Outages	205 m	111 m	113 m

this noise reduction. The difference between the CAI INS and navigation grade INS are passed though a moving average filter. This estimates the navigation grade biases and these biases are subtracted from the difference of the CAI INS and navigation grade INS measurements. This leaves an estimate of the navigation grade white noise which is removed prior to mechanization. This method is simplistic and would have to be modified to work in real time. It was used as a proof of concept to test if a filter framework could be implemented that worked better than Frameworks 1 and 2 regardless of outage times.

4.4   Dual INS Framework 3 Results

The third filter framework showed nearly identical performance to Framework 2. The results of the Framework 3 testing is shown in Table 4.7. It can be seen that the third Framework is not improving performance over Framework 2. Even with the VRW and ARW noise reduction, it is still not as accurate as Framework 1 for short outages. To test why this was occurring, a time correlated bias only case was tested with an 80 percent duty cycle. It can be seen from this case that the errors are nearly identical to the normal 80 percent duty cycle case. This indicates that the bias is strongly driving the errors, and it is not the VRW and ARW that are causing the better performance of Framework 1 under short outages. This indicates that there is another source of error in Framework 2 and 3 that is not encountered in Framework 1.

It was suspected that the remaining error between Frameworks 1 and 2 may have been by caused by differences between the Pinson error model and the INS

Table 4.8:   Comparison of Dual INS Filter Frameworks in Increased Noise Test Case

Test Case	Framework 1	Framework 2	Framework 3
97% Duty Cycle	63 m	412 m	395 m
80% Duty Cycle	181 m	423 m	391 m

mechanization equations. This was tested by running measurements with only a bias through INS mechanization equations, as well as the uncorrupted measurements. The difference in these solutions would be the error due to a bias only. The true bias was then propagated through the Pinson error model. If the Pinson error model was modeling the mechanization equations perfectly there would be no error between the results of these two simulations. In the sample run conducted there was a DRMS error of 17 meters between the mechanization equations and the Pinson error model. This error is large enough to account for the improvements in performance of Framework 1 during short outages. What exactly caused the small difference between the Pinson error model and the mechanization equations in this simulation is unknown. The Pinson error model is a first order approximation of the errors of an INS. When dealing with a navigation grade system these small errors are drowned out by other errors. Whether these errors will be important or not in a system with predicted performance of 5 meters per hour bears further study.

Framework 3 did not perform better than Framework 2 as expected. It was determined that this was because the dominant error terms were the biases. To test this concept, several simulations with increased noise were run. These simulations increased the noise by a factor of 10 and decreased the bias driving noise strength by a factor of 10. In these simulations, Framework 3 performed better than Framework 2. The results of these simulations are shown in Table 4.8. Interestingly, while Framework 3 does now perform better than Framework 2, Framework 1 has the lowest error by far. When the biases become much smaller relative to the white noise, as was the case in these simulations, the filter's estimates of the biases are no longer as accurate. Because of this, Framework 1, which mechanizes off of the CAI INS measurements whenever they are available, performs better. Any errors in the bias estimate only

Table 4.9:   Comparison of Two Frameworks When Integrating CAI INS with a Tactical Grade INS, 10 MC Runs, Nominal Case

Framework	DRMS Error (km)
1	27.3 km
2	24.9 km

accumulate during outages in Framework 1. This reveals a further tradeoff between the various filter frameworks. Using the predicted CAI INS performance given in [5], Frameworks 2 and 3 perform the best in all but very short outage cases where modeling error makes Framework 1 better. If, however, the bias states do not have as good observability as they do using the predicted performance used in this simulation, Framework 1 may be better.

4.5   Framework 1 and 2 Performance with CAI-Tactical Grade INS Integration

The performance of both Frameworks integrated with a tactical grade system was tested. Previously it was shown that the two frameworks had similar performance for the CAI-Nav grade INS integration. The first framework is able to reduce velocity and angular random walk errors. These errors are not corrected in Framework 2. A simulation was run to explore if it is feasible to integrate a CAI INS with a tactical grade INS. The VRW and ARW errors are unacceptably high in a tactical grade system, so it is anticipated that Framework 2 will not work. Simulations were run to test if Framework 1 could have acceptable performance with a CAI INS - tactical grade INS integration. Table 4.5 shows the performance of the two frameworks under the nominal condition. It can be seen that the errors are unacceptably high for both Frameworks. Tactical INS errors are simply too high for the CAI system to fully correct. Even with the reduction of white noise in the first framework the other errors are too high. The first framework did perform better, as expected, but neither performed well enough in the simulations to be used for navigation.

4.6   GPS-CAI Integration Results

The increased accuracy of the CAI system allows for long GPS outages. Example plots show the system errors for a CAI system with accuracy given in [5] and a measurement frequency of 5 seconds and 1000 seconds. For comparison, a navigation grade system was aided in the same way with the same measurements. The accuracy of the GPS measurements had a standard deviation of 3 meters. Fig 4.30 shows east errors for both a CAI and a Nav grade GPS aided system with a outage time of 5 seconds. Fig 4.31 shows east errors for both a CAI and a Nav grade GPS aided system with a outage time of 1000 seconds. Fig 4.32 shows the CAI solution from Fig 4.31 enlarged. Fig 4.33 shows the filter estimation of the measurement bias. Table 4.6 shows the Monte Carlo RMS errors for various GPS measurement frequencies. It can be seen that the CAI INS errors drift much slower than a conventional INS, as expected. This allows the CAI INS-GPS to experience outages much longer than the conventional INS-GPS. The most frequent GPS measurements were taken at 5 second intervals. At this rate the CAI INS kept the error near zero and the navigation grade INS error bounded by the standard deviation of the GPS measurements, which was 3 meters. When outage times were increased to 1000 seconds the navigation grade INS drifted up to 2000 meters. The CAI INS-GPS kept the errors below 25 meters. This is a significant increase in accuracy. To have this same accuracy for a conventional INS the outage times must be ten times shorter.

Table 4.10:   CAI-GPS Monte Carlo RMS Error with Varying Measurement Availability

| Measurement Interval	CAI DRMS Error (m)	Nav DRMS Error (m)	Improvement Factor
5 sec	0.01	2.49	249
10 sec	0.01	2.93	293
20 sec	0.01	3.66	366
50 sec	0.02	5.69	284
100 sec	0.12	10.06	84
200 sec	0.45	26.9	60
500 sec	2.74	178.74	65
1000 sec	8.50	646.80	76
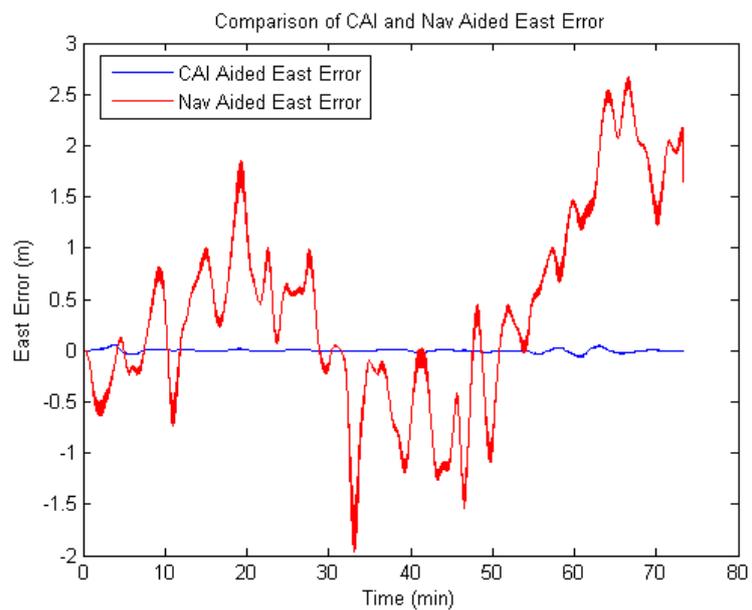
Figure 4.30:   Comparison of East Errors for a CAI and Nav Aided GPS-INS System with Outage Time=5 Seconds
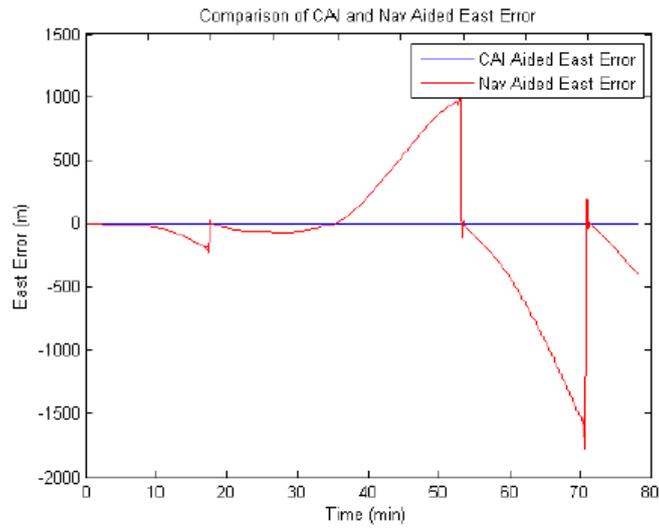
Figure 4.31:   Comparison of East Errors for a CAI and Nav Aided GPS-INS System with Outage Time=1000 Seconds
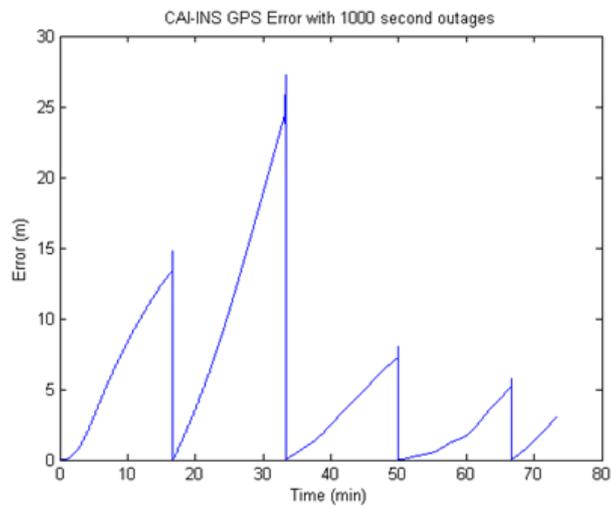

Figure 4.32:   Comparison of East Errors for a CAI and Nav Aided GPS-INS System with Outage Time=1000 Seconds
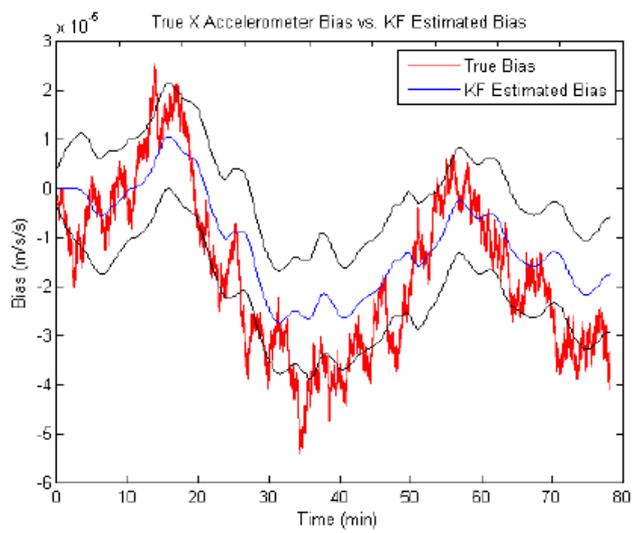
Figure 4.33: GPS-INS Estimate of Navigation-Grade Bias with a CAI-GPS System For a Single Run

V. Conclusions and Recommendations

5.1 Conclusions

5.1.1 Dual INS Integrations. The first goal of this research was to explore methods of integrating CAI INS with a navigation grade INS. Three different methods were tested and compared for integrating a CAI INS with a navigation grade INS. These methods were tested in a full six degree of freedom simulation environment using a realistic flight trajectory. The simulation environment for the dual INS integration created frequent periodic and g-induced outages of the CAI INS. Under short outages Framework 1, which mechanized at the measurement level, performed best. This was due to modeling error of the mechanization equations. The exact cause of the modeling error was not determined but could be sampling issues or the first order approximations of the Pinson error model. With longer outages, including the realistic g-induced outage cases, Framework 2 performed the best. The benefits gained by using the Pinson error model are apparent when comparing the performance of Frameworks 1 and 2. These frameworks estimate the navigation grade errors the same way. This indicates the improvements in accuracy come from the corrections to the attitude, velocity, and position states of the Pinson error model. These states are adjusted with returning CAI INS measurements because of the cross correlation between the bias states and the Pinson error model states. In the 3-g induced outage case, which experienced outages 27% of the time, the DRMS error was 111 meters. Even though the highly accurate CAI INS measurements were used only two thirds of the flight there is still significant improvement over the nautical mile per hour performance of a navigation grade system.

The third framework did not improve performance over the second framework as hoped. This was determined to be caused by the fact that the bias errors were the driving error sources in the simulation, and errors caused by white noise were drowned out by these errors. This was verified by increasing the noise and decreasing the bias driving noise strength. In these higher noise simulations Framework 3 had better performance than Framework 2. Both frameworks, however, performed worse

than Framework 1 in these high noise simulations, due to the decreased observability of the bias. When the bias estimate is poor the use of the CAI INS measurements whenever they are available is the best approach.

The simulations in this research show that integrating CAI INS with navigation grade INS is an effective way to address the dynamic limitations of a CAI INS. The tradespace study done shows that under a wide range of CAI INS accuracies and dynamic performances the dual INS system still performs much better than a navigation grade system alone. The CAI INS is accurate enough to estimate and correct many of navigation grade INS errors, although not all errors are observable. These estimates create a well calibrated navigation grade system which will give much better performance than an un-calibrated navigation grade system. The navigation grade INS allows the system to perform under a much higher range of dynamics than the CAI INS could alone. It can be seen from the simulations that the navigation grade INS is the limiting factor for performance. Increasing the accuracy of the CAI INS over the predicted performance given in [5] does not improve navigation accuracy.

5.1.2 CAI INS Integration With Tactical Grade INS.   The feasibility of integrating a CAI INS with a tactical grade INS was tested. It was thought that the use of the CAI INS measurements the majority of the time would allow this integration to be possible. During outages of the CAI INS, however, the error simply grows too quickly. Neither framework performed well enough with a tactical level system to be useful for navigation, although other methods of integrating with a tactical grade system could be more successful.

5.1.3 CAI INS Integration with GPS.   The integration of a CAI INS system with GPS was conducted to show the performance benefits of a CAI grade INS system over a navigation grade system. The simulation environment created various length GPS outages to compare the two INS systems. The smallest improvement occurred with 200 second outages and improved performance by a factor of 60. The best improvement occurred with outages of 20 seconds and improved performance by a

factor of 366. Furthermore, the max error of the CAI systems experiencing 1000 second outages was still less than 10 meters. This is significant because the system is keeping near GPS level accuracy even with significant outages. That same accuracy with a navigation grade INS-GPS implementation requires outages to be no greater than 10 seconds. This indicates that in an environment vulnerable to GPS outages, using a CAI grade INS system gives significant performance improvements.

5.2 *Future Work Recommendations*

The simulations conducted here were done using a single flight path trajectory. While realistic, many effects of a navigation system are trajectory dependent. Future work could focus on testing these filter implementations in a variety of flight trajectories. Also, information on the performance of CAI systems is still fairly new, as well as the dynamic performance limitations. When these system parameters become better known, more concrete numbers may be determined for the performance of CAI INS systems integrated with other sensors. Another simulation that could be looked at is the integration of a CAI INS system with an additional CAI INS system. To address the trade space considerations, the CAI INS systems could be tuned to have one perform high level flight accuracy and another to perform well under high dynamics. Finally, flight testing of an actual CAI INS system integrated with other sensors could be performed in the future.

Bibliography

1. Allerton and Jia. An error compensation method for skewed redundant inertial configuration. In *Proceedings of the 58th Annual Meeting of The Institute of Navigation and CIGTF 21st Guidance Test Symposium*, pages 142 – 147, Albuquerque, NM, June 2002. Institute of Navigation.

2. J.B. Bancroft. Data fusion algorithms for multiple inertial measurement units. *Sensors*, (11):6771–6798, 2011.

3. G. Foster T. Gustavson A. Landragin J. McGuirk M. Kasevich D. Durfee, J. Fixler. Atom interferometer inertial force sensors. In *Position Location and Navigation Symposium*, San Diego, CA, Mar 2000. IEEE.

4. Dale Arden Jeff Bird, J. Chris McMillan. A highly fault tolerant, dual inertial integrated navigation system (diins). In *Proceedings of the 1992 National Technical Meeting of The Institute of Navigation*, pages 235–244, San Diago, CA, January 1992.

5. Christopher Jekeli. Navigation error analysis of atom interferometer inertial sensor. *Institute of Navigation (ION)*, 52(1):1–14, spring 2005.

6. Peter S. Maybeck. *Stochastic Models, Estimation, and Control Volume 1*. NavTech Book and Software Store, Arlington, VA, 1994.

7. Holger Muller. A precision measurement of the gravitational redshift by the interference of matter waves. *Nature*, 463:926–929, 2010.

8. Jonathan M. Neu. A tightly coupled ins/gps using a mems imu. Master's thesis, Graduate School of Engineering, Air Force Institute of Technology (AETC), Wright-Patterson AFB OH, September 2004. AFIT/GE/ENG/04-19.

9. George T. Schmidt. Ins/gps integration architectures. Technical Report RTO-EN-SET-064, The Charles Stark Draper Laboratory, Cambridge, MA.

10. D.H. Titterton and Weston. *Strapdown inertial navigation technology*. Peter Peregrinus Ltd., London, England, 1997.

11. Michael J. Veth. *Fusion of Imaging and Inertial Sensors for Navigation*. Ph.d. dissertation, Graduate School of Engineering, Air Force Institute of Technology (AETC), Wright-Patterson AFB OH, September. AFIT/DS/ENG/06-09.

12. Adrian Waegli. Noise reduction and estimation in multiple micro-electro-mechanical inertial systems. *Measurement Science and Technology*, (21):6, March 2010.

13. John H. Wall Warren S. Flenniken IV and David M. Bevly. Characterization of various imu error sources and the effect on navigation performance. In *Proceedings of the 18th International Technical Meeting of the Satellite Division of The Institute of Navigation (ION GNSS 2005)*, Long Beach, CA, September 2005.

REPORT DOCUMENTATION PAGE

Form Approved
OMB No. 0704–0188

1. REPORT DATE *(DD–MM–YYYY)*	2. REPORT TYPE	3. DATES COVERED *(From — To)*
22–03–2012	Master's Thesis	Aug 2010 — Mar 2012

4. TITLE AND SUBTITLE

Integration of Cold
Atom Interferometry INS
with Other Sensors

5a. CONTRACT NUMBER

5b. GRANT NUMBER

5c. PROGRAM ELEMENT NUMBER

6. AUTHOR(S)

Canciani, Aaron J., 2Lt, USAF

5d. PROJECT NUMBER

12G397A

5e. TASK NUMBER

5f. WORK UNIT NUMBER

7. PERFORMING ORGANIZATION NAME(S) AND ADDRESS(ES)

Air Force Institute of Technology
Graduate School of Engineering and Management (AFIT/EN)
2950 Hobson Way
WPAFB OH 45433-7765

8. PERFORMING ORGANIZATION REPORT NUMBER

AFIT/GE/ENG/12-07

9. SPONSORING / MONITORING AGENCY NAME(S) AND ADDRESS(ES)

Jacob Cambell
4421 Avionics Circle
Wright Patterson AFB, OH 45433
(937) 255-6127 x4154 Jacob.Campbell@wpafb.af.mil

10. SPONSOR/MONITOR'S ACRONYM(S)

AFSEO

11. SPONSOR/MONITOR'S REPORT NUMBER(S)

12. DISTRIBUTION / AVAILABILITY STATEMENT

Approval for public release; distribution is unlimited.

13. SUPPLEMENTARY NOTES

This material is declared a work of the U.S. Government and is not subject to copyright protection in the United States.

14. ABSTRACT

Inertial navigation systems (INS) using cold-atom interferometry are currently under development, and sensors in these systems are expected to be several orders of magnitude more ccurate than current navigation grade sensors. This significant increase in accuracy motivates the need to explore how these high accuracy inertial navigation systems can be integrated with other sensors. This research focuses on methods of integrating cold atom interferometry INS with conventional navigation grade INS, as well as with GPS. Results from a full 6 degree of freedom simulation show that integrating CAI INS with navigation grade INS is a successful way to address the dynamic performance limitations of a CAI INS. Results from a CAI INS-GPS simulation show that a CAI INS-GPS can keep near GPS level accuracy with outages as long as 1000 seconds, compared to 100 seconds with a navigation grade INS.

15. SUBJECT TERMS

Dual INS Integration, Cold Atom Interferometry, INS-GPS Integration

16. SECURITY CLASSIFICATION OF:			17. LIMITATION OF ABSTRACT	18. NUMBER OF PAGES	19a. NAME OF RESPONSIBLE PERSON
a. REPORT	b. ABSTRACT	c. THIS PAGE			Dr John Raquet
U	U	U	UU	102	19b. TELEPHONE NUMBER *(include area code)* (937) 785-3636, ext 4580; john.raquet afit.edu

Standard Form 298 (Rev. 8–98)
Prescribed by ANSI Std. Z39.18